Integrated studies of a regional ozone pollution synthetically affected by subtropical high and typhoon system in the Yangtze River Delta region, China

Lei Shu[*], Min Xie[*], Tijian Wang[*], Da Gao, Pulong Chen, Yong Han, Shu Li, Bingliang Zhuang, Mengmeng Li

School of Atmospheric Sciences, CMA-NJU Joint Laboratory for Climate Prediction Studies, Jiangsu Collaborative Innovation Center for Climate Change, Nanjing University, Nanjing 210023, China

----

*Correspondence to: Min Xie (minxie@nju.edu.cn) and Tijian Wang (tjwang@nju.edu.cn)

Abstract: Severe high ozone (O_3) episodes usually have close relations to synoptic systems. A regional continuous O_3 pollution episode was detected over the Yangtze River Delta (YRD) region in China during August 7-12 2013, in which the O_3 concentrations in more than half of the cities exceeded the national air quality standard. The maximum hourly concentration of O_3 reached 167.1 ppb. By means of the observational analysis and the numerical simulation, the characteristics and the essential impact factors of the typical regional O_3 pollution are integratedly investigated. The observational analysis shows that the atmospheric subsidence dominated by Western Pacific subtropical high plays a crucial role in the formation of high-level O_3. The favorable weather conditions, such as extremely high temperature, low relative humidity and weak wind speed, caused by the abnormally strong subtropical high are responsible for the trapping and the chemical production of O_3 in the boundary layer. In addition, when the YRD cities at the front of Typhoon Utor, the periphery circulation of typhoon system can enhance the downward airflows and cause worse air quality. But when the typhoon system weakens the subtropical high, the prevailing southeasterly surface wind leads to the mitigation of the O_3 pollution. The Integrated Process Rate (IPR) analysis incorporated in the Community Multi-scale Air Quality (CMAQ) Model is applied to further illustrate the combined influence of subtropical high and typhoon system in this O_3 episode. The results show that the vertical diffusion (VDIF) and the gas-phase chemistry (CHEM) are two major contributors to O_3 formation. During the episode, the

30   contributions of VDIF and CHEM to O_3 maintain the high values over the YRD region. On August

31   10-12, the cities close to the sea are apparently affected by the typhoon system, with the

32   contribution of VDIF increasing to 28.45 ppb/h in Shanghai and 19.76 ppb/h in Hangzhou. In

33   contrast, the cities far away from the sea can hardly be affected by the periphery circulation of

34   typhoon system. When the typhoon system significantly weakens the subtropical high, the

35   contribution values of all individual processes decrease to a low level in all YRD cities. These

36   results provide an insight for the O_3 pollution synthetically impacted by the Western Pacific

37   subtropical high and the tropical cyclone system.

38   **Keyword**: Ozone; subtropical high; typhoon; the Yangtze River Delta region; heat wave

39

40   **1. Introduction**

41   Ground-level ozone (O_3) is a secondary air pollutant generated by a series of complicated

42   photochemical reactions involving nitrogen oxides (NO_x) and hydrocarbons (HC) (Crutzen, 1973;

43   Sillman, 1999; Jenkin et al., 2000; Wang et al., 2006b; Xie et al., 2014; 2016b). Severe O_3

44   pollution events usually occur in the presence of sunlight and under favorable meteorological

45   conditions, with the abundance of O_3 precursors (NO_x and HC) (Wang et al., 2006b). These O_3

46   pollutions in troposphere can deteriorate the air quality, and thereby cause adverse effects on

47   human health and vegetation (Feng et al., 2003; Fann and Risley, 2013; Landry et al., 2013).

48   Consequently, the formation mechanism and the integrated prevention of O_3 pollution are of great

49   concern in many megacities all over the world (Xie et al., 2016b).

50   Over the past decades, along with the rapid industrial and economic development, many areas

51   in China have been suffering from high levels of O_3 pollution. Especially in the most economically

52   vibrant and densely populated areas, such as the Yangtze River Delta (YRD) region, the Pearl

53   River Delta (PRD) region, and the Beijing-Tianjin-Hebei (BTH) area, the severe O_3 pollution

54   episode has frequently occurred (Lam et al., 2005; Wang et al., 2006b; An et al., 2007; Chan and

55   Yao, 2008; Duan et al., 2008; Jiang et al., 2008; Zhang et al., 2008; Guo et al., 2009; Shao et al.,

56   2009; Ma et al., 2012) , and the background air pollutant concentrations have steadily increased

57   (Chan and Yao, 2008; Zhang et al., 2008; Tang et al., 2009; Wang et al., 2009a; Ma et al., 2012;

58   Liu et al., 2013). Many studies on the O_3 pollution, including satellite data analyses, field

59   experiments, and model simulations, have been carried out over China in order to investigate the

temporal and spatial characteristics of surface photochemical pollutions (Lu and Wang, 2006; Wang et al., 2006a; Tu et al., 2007; Zhang et al., 2007; 2008; Geng et al., 2008; Tang et al., 2008; 2009; Chen et al., 2009; Han et al., 2011; Ding et al., 2013; Xie et al., 2016b), nonlinear photochemistry of O_3 and its precursors (Lam et al., 2005; Ran et al., 2009; Liu et al., 2010; Li et al., 2011; Xie et al., 2014), interactions between O_3 and aerosols (Lou et al., 2014; Shi et al., 2015), the effects of urbanization on O_3 formation (Wang et al., 2007; 2009b; Liao et al., 2015; Li et al., 2016; Xie et al., 2016a; Zhu et al., 2016), and other essential impact factors (Jiang et al., 2012; Li et al., 2012; Wei et al., 2012; Liu et al., 2013; Gao et al., 2016).

The Yangtze River Delta (YRD) region is a highly developed area of urbanization and industrialization. With the accelerated economic development and remarkable increase in energy consumption, the photochemical smog with high level of O_3 concentration is becoming more and more prominent and frequent, tending to present the characteristics of regional pollution (Chan and Yao, 2008; Ma et al., 2012; Li et al., 2012). Being located on the southeastern coast of China, YRD features a typical subtropical monsoon climate and is strongly affected by the Western Pacific subtropical high in summer. So, high O_3 concentrations are usually observed in late spring and summer by in-situ monitoring (Ding et al., 2013; Xie et al., 2016b). Severe high O_3 episodes usually have close relations to synoptic systems (Huang et al., 2005; 2006; Wang et al, 2006b; Jiang et al., 2008; Cheng et al., 2014; Hung and Lo, 2015). Horizontal and vertical transport processes from upwind O_3-rich air masses as well as poor atmospheric diffusion conditions can lead to the accumulation of surface O_3 concentrations and aggravating the photochemical pollution (Wang et al., 2006b). In previous studies on high O_3 pollution in the YRD region, some researchers have discussed this issue. For example, Jiang et al. (2012) investigated the spring O_3 formation over East China, and suggested that O_3 concentrations over the YRD region were transported and diffused from surrounding areas. Li et al. (2012) presented quantitative analysis on atmospheric processes affecting O_3 concentrations in the typical YRD cities during a summertime regional high O_3 episode, and found that the maximum concentration of photochemical pollutants was usually related with the process of transportation. Gao et al. (2016) evaluated the O_3 concentration during a frequent shifting wind period, and revealed that vertical mixing played an important positive role in the formation of surface O_3. However, these investigations only focused on the O_3 formation mechanism for one megacity (such as Shanghai, Nanjing and Hangzhou, etc.)

90 or just a single station. Up to now, studies on the process analysis of high ozone episodes over the

91 YRD are quite limited (Li et al., 2012). So, more studies should pay attention to the typical

92 weather systems and the exact formation mechanism of the regional O_3 pollution in this region.

93   During August 7-12 2013, there was a typical regional O_3 pollution episode in the YRD

94 region, which might be synthetically influenced by the Western Pacific subtropical high and

95 Typhoon Utor. To better understand the important factors impacting O_3 formation from the

96 regional scale, we investigated the exact roles of these two typical weather systems in this

97 pollution episode by using observational analysis and numerical simulations. The observational

98 analysis was performed to identify the temporal and spatial characteristics of the episode. The

99 WRF/CMAQ model system, which consists of the Weather Research and Forecasting model

100 (WRF) and the Community Multi-scale Air Quality Model (CMAQ), were used to reveal the exact

101 formation mechanism. With the aid the Integrated Process Rate (IPR) analysis coupled in CMAQ,

102 the qualitative and the quantitative analysis on the contributions of individual atmospheric

103 processes were conducted as well. In this paper, the brief description of observational data and

104 model configurations are shown in Section 2. The detailed observational analysis of air quality and

105 meteorological conditions are given in Section 3. The evaluation of model performance and the

106 formation mechanism of O_3 explored by IPR technique are presented in Section 4. In the end, a

107 summary of main findings is given in Section 5.

108

109 **2. Methodology**

110 **2.1 Observed meteorological and chemical data**

111   The air quality observational data are used to identify the regional characteristics of the O_3

112 episode in August 2013. Fifteen cities are selected as the representative research objects to better

113 reflect the status of O_3 pollution over the YRD region. The locations of these cities are shown in

114 Fig. 1b, which contains Shanghai, 8 cities in Jiangsu province (Changzhou, Nanjing, Nantong,

115 Suzhou, Taizhou, Wuxi, Yangzhou, and Zhenjiang), and 6 cities in Zhejiang province (Hangzhou,

116 Huzhou, Jiaxing, Ningbo, Shaoxing, and Zhoushan). The in-situ monitoring data for the hourly

117 concentrations of O_3, CO, NO_2, SO_2, $PM_{2.5}$ and PM_{10} can be acquired from National

118 Environmental Monitoring Center (NEMC) (http://106.37.208.233:20035). The assurance/quality

119 control (QA/QC) procedures for monitoring strictly follow the national standards (State

120   Environmental Protection Administration of China, 2006). The hourly pollutant concentration for

121   a city is calculated as the average of the pollutant concentrations from several national monitoring

122   sites in that city, which can better characterize the pollution level of the city. In order to identify

123   invalid or lacking data, a checking procedure for these data is performed following the work of

124   Chiqueto and Silva (2010). Finally, only less than 0.2% of the primary data are ignored in the

125   calculation. Moreover, the observed data of total VOCs (TVOC) during August 4-10 at an urban

126   site in Shanghai (SAES, 31.17°N, 121.43°E) is also used. They are provided by Shanghai

127   Academy of Environmental Sciences. The sampling height is about 15 m, and individual VOC

128   species are continuously measured every 30 min by two on-line high performance gas

129   chromatograph with flame ionization detector (GC-FID) systems (Chromato-sud airmoVOC

130   C2-C6 #5250308 and airmoVOC C6-C12 #2260308, France). The details for measurement and

131   QA/QC can refer to Wang et al. (2013).

132   The weather charts and the observed surface meteorological records are used to analyze the

133   synoptic systems during the episode. The weather charts for East Asia are accessible from Korea

134   Meteorological Administration (http://www.kma.go.kr/chn/weather/images/analysischart.jsp). The

135   hourly meteorological data at the observation sites of SH (31.40°N, 121.46°E) located in Shanghai,

136   HZ (30.23°N, 120.16°E) in Hangzhou, and NJ (32.00°N, 118.80°E) in Nanjing can be obtained

137   from the University of Wyoming (http://weather.uwyo.edu/wyoming/), where 2-m air temperature,

138   2-m relative humidity, 10-m wind speed and 10-m wind direction are available.

139   Meteorological and air quality observation data are also used to validate the reliability of

140   simulations in this study. Comparisons of the modeling results with the observation data are

141   performed in Shanghai, Nanjing, and Hangzhou. Shanghai is the most populous city in China, and

142   also a global financial and transportation center. Locating to the northwest of Shanghai, Nanjing is

143   the capital of Jiangsu Province and the second largest commercial center in East China. Hangzhou

144   is the capital of Zhejiang Province and located to the southwest of Shanghai. These cities are the

145   provincial capitals and the typical metropolis in the YRD region. They are highly urbanized and

146   industrialized, and all suffer from severe O_3 pollution.

147

148   **2.2 Model description and configurations**

149   In this study, WRF/CMAQ, which consists of WRF model version 3.4.1 and CMAQ Model

150   version 4.7.1, is applied to simulate the high O_3 episode over the YRD region in August 2013.

151   Developed at the National Center for Atmospheric Research (NCAR), WRF is a new generation of

152   meso-scale weather forecast model and assimilation system. Numerous applications have proven

153   that it shows a good performance in all kinds of weather forecasts and has broad application

154   prospects in China (Jiang et al., 2008; 2012; Wang et al., 2009b; Liu et al., 2013; Xie et al., 2014;

155   2016a; Liao et al., 2014; 2015; Li et al., 2016; Zhu et al., 2016). WRF provides off-line

156   meteorological fields as the input for the chemical transport model CMAQ. CMAQ is a third

157   generation of regional air quality model developed by the Environmental Protection Agency of

158   USA (USEPA). A set of up-to-date compatible modules and control equations for the atmosphere

159   is incorporated in the model, which can fully consider atmospheric complicated physical processes,

160   chemical processes and the relative contribution of different species (Byun and Schere, 2006;

161   Foley et al., 2010). CMAQ has been widely applied in China and proven to be a reliable tool in

162   simulating air quality from city scale to meso scale (Li et al., 2012; Wei et al., 2012; Liu et al.,

163   2013; Zhu et al., 2016).

164   The simulation run is conducted from 08:00 (local standard time, LST) on August 2 to 08:00

165   (LST) on August 16 2013, in which the first 48 h is taken as the spin-up time. Three one-way

166   nested domains are used in WRF with a Lambert Conformal map projection. The domain setting is

167   shown in Fig. 1. The outermost domain (domain 1, d01) covers the most areas of East Asia and

168   South Asia, with the horizontal grids of 88×75 and the grid spacing of 81km. The nested domain

169   d02 covers the southeastern part of China, with the horizontal grids of 85×70 and the grid spacing

170   of 27km. The finest domain (domain 3, d03) covers the core areas of the YRD region, with the

171   grid system of 70×64 and the resolution of 9km. For all domains, there are 23 vertical sigma

172   layers from the surface to the top pressure of 100hPa, with about 10 layers in the planetary

173   boundary layer. The detailed configuration options for the dynamic parameterization in WRF are

174   summarized in Table 1. Additionally, the SLAB scheme that does not consider urban canopy

175   parameters is adopted to model the urban effect. In order to reflect the rapid urban expansion in

176   the YRD region, the default United States Geological Survey (USGS) land-use archives are

177   updated by adding the present urban land-use conditions from 500-m Moderate Resolution

178   Imaging Spectroradiometer (MODIS) data, based on the work of Liao et al. (2014; 2015). The

179   initial meteorological fields and boundary conditions are from 1° resolution global reanalysis data

180 provided by National Center for Environmental Prediction (NCEP). The boundary conditions are

181 forced every 6 h.

182
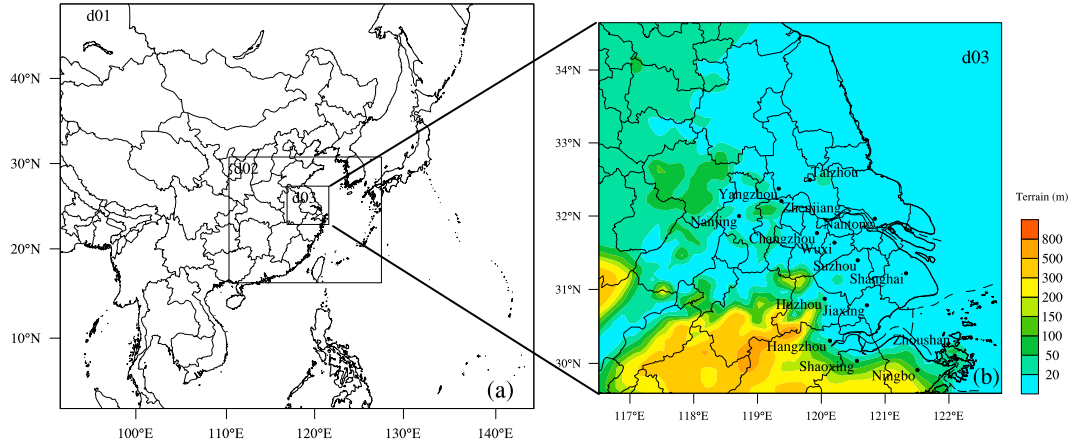
183

184 **Fig. 1. Domain settings, include (a) the three nested modeling domains and (b) the nested domain 3 (d03)**

185 **with the terrain elevations and the locations of 15 main cities in the YRD region.**

186

187 **Table 1. The grid settings and the physical options for WRF in this study.**

Items	Options
Dimensions (x, y)	(88, 75), (85, 70), (70, 64)
Grid spacing (km)	81, 27, 9
Microphysics	WRF Single-Moment 5-class scheme (Hong et al., 2004)
Longwave Radiation	RRTM scheme (Mlawer et al., 1997)
Shortwave Radiation	Goddard scheme (Kim and Wang, 2011)
Surface layer	Moni-Obukhov scheme (Monin and Obukhov, 1954)
Land-surface layer	Noah Land Surface Model (Chen and Dudhia, 2001)
Planetary Boundary layer	YSU scheme (Hong et al., 2006)
Cumulus Parameterization	Grell-Devenyi ensemble scheme (Grell and Devenyi, 2002)

188

189 With respect to the air quality model, CMAQ uses the same vertical levels and the similar

190 three nested domains as those adopted in the meteorological simulation, whereas the CMAQ

191 domains are one grid smaller than the WRF domains. The Meteorology Chemistry Interface

192 Processor (MCIP) is used to convert WRF outputs to the input meteorological files needed by

193 CMAQ. The Carbon Bond 05 chemical mechanism (CB05) (Yarwood et al., 2005) is chosen for

194 gas-phase chemistry, and the 4rd generation CMAQ aerosol module (Byun and Schere, 2006) is

195 adopted for aerosol chemistry. The initial and outmost boundary conditions are obtained from the

196   Model for Ozone and Related Chemical Tracers version 4 (MOZART-4) (Emmons et al., 2010),

197   while those for the two nested inner domains are extracted from the immediate concentration files

198   of their parent domains. The anthropogenic emissions are mainly from the 2012 Multi-resolution

199   Emission Inventory for China (MEIC) with $0.25° \times 0.25°$ resolution, which is re-projected for the

200   grids of China in both domains. For the grids outside of China, the inventory developed for the

201   Intercontinental Chemical Transport Experiment-Phase B (INTEX-B) by Zhang et al. (2009) is

202   used. The natural O_3 precursor emissions are calculated by the natural emission model developed

203   by Xie et al. (2007; 2009; 2014), including NO from soil, VOCs from vegetations, and CH_4 from

204   rice paddies and terrestrial plants. The biomass burning emissions are acquired from the work of

205   Xie et al. (2014; 2016a).

206   **2.3 Integrated Process Rate (IPR) analysis method**

207   The CMAQ modeling system contains process analysis module (PROCAN), which consists

208   of the Integrated Process Rate (IPR) analysis and the Integrated Reaction Rate (IRR) analysis

209   (Byun and Schere, 2006). IPR has the capability of calculating the hourly contributions of

210   individual physical processes and the net effect of chemical reaction compared to the overall

211   concentrations, and thereby can determine the quantitative contribution of each process in a

212   specific grid cell. The atmospheric processes considered in IPR include the horizontal advection

213   (HADV), the vertical advection (ZADV), the horizontal diffusion (HDIF), the vertical diffusion

214   (VDIF), the emissions (EMIS), the dry deposition (DDEP), the cloud processes with the aqueous

215   chemistry (CLDS), the aerosol processes (AERO) and the gas-phase chemistry (CHEM). IPR has

216   been widely applied to investigate the regional photochemical pollutions, and proven to be an

217   effective tool to show the relative importance of every process and provide a fundamental

218   interpretation (Goncalves et al., 2009; Li et al., 2012; Liu et al., 2013; Zhu et al., 2016). In this

219   paper, the period from August 4 to 15 is selected for the IPR analysis. With the aid of IPR, we

220   assess the roles of the individual physical and chemical processes involved in O_3 formation over

221   the YRD region, and further present those in the typical cities (Shanghai, Nanjing and Hangzhou).

222   **2.4 Evaluation method**

223   Comparisons of the modeling results in the finest domain (d03) with the hourly observation

224   data are performed for meteorological factors and air pollutants in Shanghai, Hangzhou, and

225   Nanjing. The correlation coefficient (R), the normalized mean bias (NMB) and the

226 root-mean-square error (RMSE) are used to evaluate the model performance. These statistic values

227 are calculated as follows:

228
$$R = \frac{\sum_{i=1}^{N}(S_i - \bar{S})(O_i - \bar{O})}{\sqrt{\sum_{i=1}^{N}(S_i - \bar{S})^2}\sqrt{\sum_{i=1}^{N}(O_i - \bar{O})}} \qquad (1)$$

229
$$NMB = \frac{\sum_{i=1}^{N}(S_i - O_i)}{\sum_{i=1}^{N}O_i} \times 100\% \qquad (2)$$

230
$$RMSE = [\frac{1}{N}\sum_{i=1}^{N}(S_i - O_i)^2]^{\frac{1}{2}} \qquad (3)$$

231 where S_i and O_i represent the simulated and the observed value, respectively. N means the total

232 number of valid data. Generally, the model performance is acceptable if the values of NMB and

233 RMSE are close to 0 and that of R is close to 1.

234

235 **3. Characteristics of the continuous ozone episode**

236 **3.1 Basic characteristic of the regional ozone episode in August 2013**

237 Fig. 2 shows the temporal variation of the hourly O_3 concentrations observed in 15 typical

238 cities over the YRD region from 00:00 (Universal Time Coordinated, UTC) August 4 to 23:00

239 (UTC) August 15 in 2013. Obviously, from August 7 to 12, high O_3 concentrations over 93.5 ppb

240 (approximately equal to the hourly national air quality standard of 200 μg/m^3) have been

241 frequently recorded in 13 cities, which means O_3 concentrations in most cities over the YRD

242 region exceed the national air quality standard. So, this high O_3 pollution episode is a typical

243 regional O_3 pollution episode that can affect the people and the ecosystem in a large area. In

244 general, for each city, there is a remarkable continuous growth in O_3 concentrations before the O_3

245 episode, followed by the lasting heavy O_3 pollution period. Though the O_3 concentrations in

246 Shaoxing and Nanjing meet the national O_3 standard, their time series still show the similar

247 tendency for the other cities in the same region. The excessive level of O_3 occurring in Huzhou,

248 Jiaxing, Nantong, Yangzhou and Shanghai lasts for more than six consecutive days, reflecting the

249 regional continuous characteristics of this O_3 pollution episode.

250 According to the temporal variation characteristics of O_3 illustrated in Fig. 2, the

251 abovementioned 15 typical YRD cities can be classified into three categories: (1) the cities in the

252   Southeast Coastal Region (SCR), including Shanghai, Suzhou, Jiaxing, Ningbo, Shaoxing, and

253   Zhoushan; (2) the cities in the Central Inland Region (CIR), including Hangzhou, Huzhou, Wuxi,

254   Changzhou, and Nantong; and (3) the cities in the Northwestern Inland Region (NIR), including

255   Nanjing, Yangzhou, Zhenjiang, and Taizhou. The classification is primarily on basis of the

256   observational facts that the maximum O_3 concentrations occur on August 10-11, 12, and 13, and

257   begin to synchronously decrease on August 12, 13 and 14 in SCR, CIR and NIR, respectively. As

258   shown in Fig. 2, in the Southeast Coastal Region (SCR), Zhoushan firstly exceeds the national O_3

259   standard on August 4, followed by Jiaxing, Shanghai, Suzhou and Ningbo. The peak hourly O_3

260   concentration of SCR occurs in Jiaxing on August 10, with the value up to 162.4 ppb. In the

261   Central Inland Region (CIR), Huzhou is the first city exceeding the national O_3 standard, followed

262   by the order of Nantong, Changzhou, Wuxi, and Hangzhou. The high-level O_3 pollution in

263   Huzhou lasts during August 5-13. In Nantong and Changzhou, the maximum hourly O_3

264   concentration reaches 167.1 ppb on August 10 and 166.1 ppb on August 12, respectively. As for

265   the Northwest Inland Region (NIR), Yangzhou, Zhenjiang, and Taizhou successively exceed the

266   national O_3 standard. It is also noteworthy that the date when O_3 concentration exceeds the

267   national air quality standard in coastal region is ahead of that in inland regions, so is the date of O_3

268   decrease. The different start time of O_3 decreasing in different regions might be related to the

269   strong southeast wind in accordance with the movement of Typhoon Utor, which is discussed in

270   Sect. 3.2 in detail.

271

272
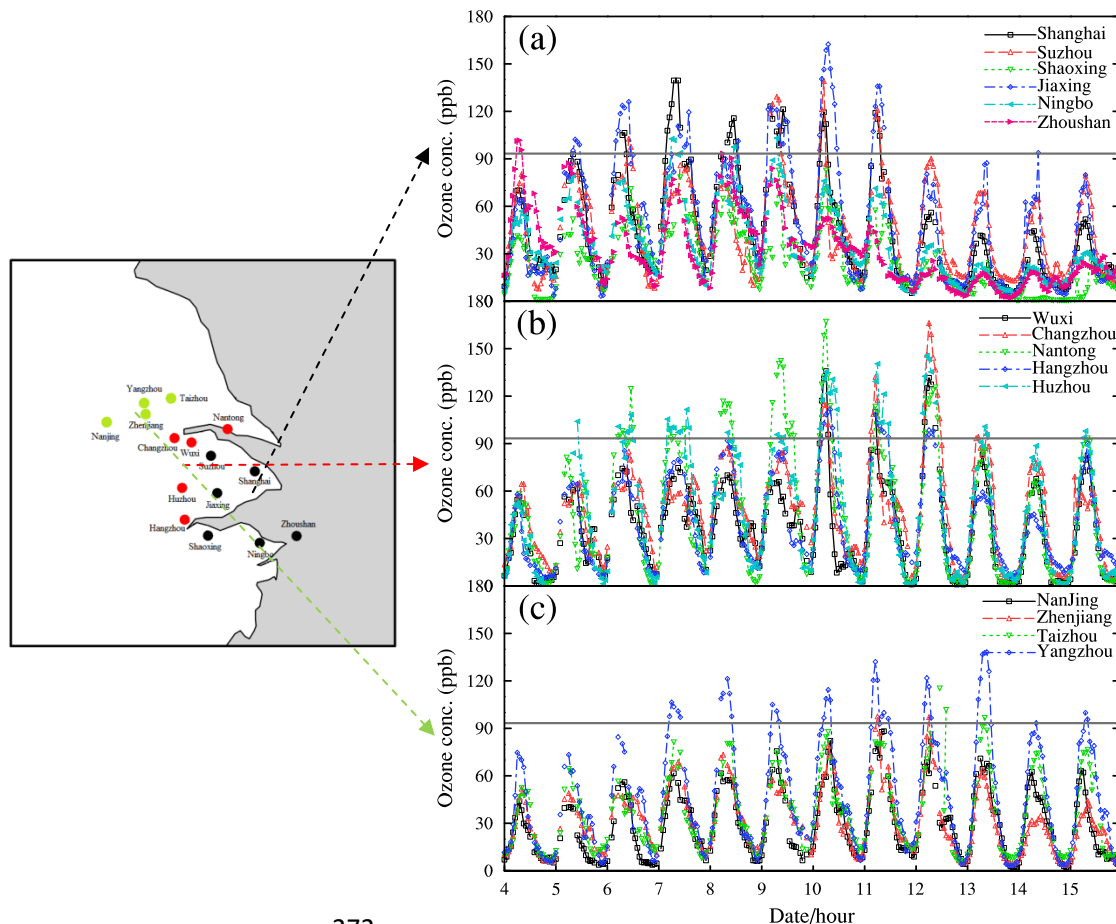
Fig. 2. The time series of the observed O₃ concentrations in 15 typical cities from August 4 to 15 2013 over the YRD region, which can be divided into three areas: (a) the Southeast Coast Region (SCR), including Shanghai, Suzhou, Shaoxing, Jiaxing, Ningbo, and Zhoushan; (b) the Central Inland Region (CIR), including Wuxi, Changzhou, Nantong, Hangzhou, and Huzhou; (c) the Northwest Inland Region (NIR), including Nanjing, Zhenjiang, Taizhou and Yangzhou. The gray solid lines in (a), (b), and (c) represent the national standard for the hourly O₃ concentration, which is 200 μg/m³.

Table 2 presents the maximum and the average concentrations of O_3 and NO_2 in 15 YRD cities during August 7-12 2013. It illustrates that the mean concentrations of NO_2 in different YRD cities range from 7.7 to 24.5 ppb during the O_3 episode, indicating the heterogeneity of the spatial distribution of O_3 precursor emissions. For O_3, the highest hourly concentration (167.1 ppb) occurs in Nantong, followed by 166.1 ppb in Changzhou and 162.4 ppb in Jiaxing. These values are all nearly 2 times of the national air quality standard. It seems that O_3 concentrations are higher in the cities around Shanghai, where the concentrations of O_3 precursors are more adequate as well. High concentrations of O_3 and its precursors imply that there may be stronger photochemical reactions.

Table 2. The maximum and average concentrations of O_3 and NO_2 observed in 15 cities during August 7-12 2013 (ppb).

Sites		O_3		NO_2	
		Max	Mean	Max	Mean
Southeast Coast Region (CSR)	Shanghai	139.5	55.1	35.1	15.6
	Suzhou	139.1	50.9	50.6	19.7
	Jiaxing	162.4	61.1	52.1	17.1
	Ningbo	113.4	41.9	31.2	12.4
	Shaoxing	82.6	31.9	27.8	12.7
	Zhoushan	93.6	35.5	27.3	7.8
Central Inland Region (CIR)	Hangzhou	111.5	48.6	30.2	16.7
	Huzhou	145.6	57.2	43.8	20.8
	Wuxi	135.8	43.2	39.9	18.8
	Changzhou	166.1	55.7	58.4	24.5
	Nantong	167.1	56.0	48.2	20.9
Northwest Inland Region (NIR)	Nanjing	88.2	34.1	41.4	21.9
	Yangzhou	132.1	54.1	36.0	17.1
	Zhenjiang	97.5	37.7	38.5	20.1
	Taizhou	115.3	40.5	18.5	7.7

Fig. 3 demonstrates the hourly variations of the observed NO_2 concentrations in Shanghai, Nanjing and Hangzhou from August 4 to 15 2013, and the time series of TVOC observed at SAES in Shanghai from August 4 to 10 2013. Obviously, there are two peaks in the diurnal cycles of NO_2 and VOC at all sites, which should be related with the rush hours in cities. The photolysis of NO_2 dominates O_3-VOC-NO_x chemistry after 8:00, and thereby makes the concentrations of precursors (NO_2 and VOC) begin to decrease. Thus, the related reactions form O_3 and increase its concentration until about 14:00. These diurnal variations of O_3 and its precursors follow the typical patterns in the polluted areas and reflect the close relationships between O_3, VOC and NO_x (Wang et al., 2013; Xie et al., 2016b). Moreover, the daily variations of NO_2 and VOC show good agreement with those of O_3. For VOC, the concentration in Shanghai largely increases since August 6, which corresponds well with the over-standard O_3 concentrations since then (Fig. 2). For NO_2, the higher values occur from August 6 to 11 in all cities, but the concentrations start to decrease on August 12, 13 and 14 in Shanghai, Hangzhou and Nanjing, respectively. It seems that the changes of O_3 precursors (NO_2 and VOC) are also affected by the movement of Typhoon Utor.

307

308
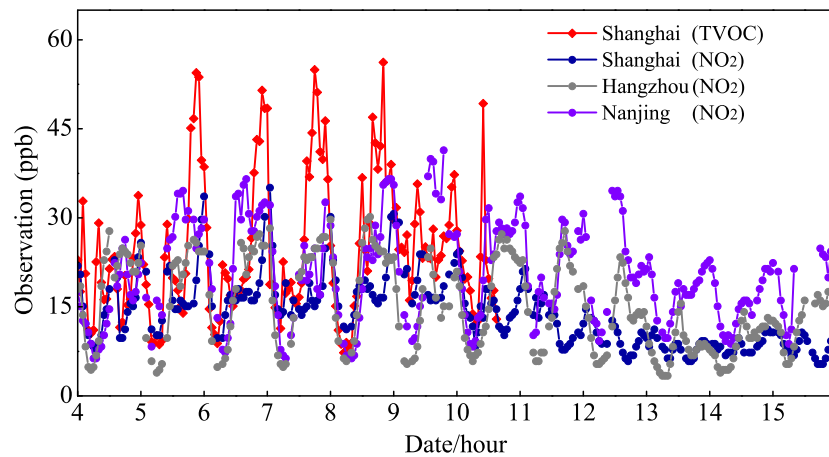
Fig. 3. Temporal variations of the observed NO$_2$ concentrations at Shanghai, Nanjing and Hangzhou stations from August 4 to 15 2013 and the observed TVOC concentration at SAES (31.17°N, 121.43°E) in Shanghai from August 4 to 10 2013.

312

3.2 Meteorological condition and its effect

Favorable weather conditions have large impacts on the formation of severe O$_3$ pollution (Huang et al., 2005; 2006; Wang et al, 2006b; Jiang et al., 2008; Cheng et al., 2014; Hung and Lo, 2015). High-level O$_3$ episodes often take place in hot seasons, when the meteorological conditions with high temperature and strong solar radiation are beneficial to the photochemical reactions of O$_3$ (Lam et al., 2005). Fig. 4 shows the variations of the surface meteorological parameters that are related to this photochemical pollution episode during August 4-15, including 2-m air temperature, 2-m relative humidity, 10-m wind speed and 10-m wind direction at the meteorological sites in Shanghai (SH) of SCR, Hangzhou (HZ) of CIR, and Nanjing (NJ) of NIR .

As shown in Fig. 4a, the hot weather at SH, HZ and NJ exists for nearly a week from August 7 to 12, with the hourly maximum temperature reaching the value over 40 $^{\circ}$C. Meanwhile, the variations of 2-m relative humidity show the negative correlation with those of 2-m air temperature. The minimum 2-m relative humidity at SH and HZ occur on August 9 and August 10 respectively, with the value below 75%. These minimum values are also lower than the values before and after the O$_3$ episode, suggesting that high-level O$_3$ episodes usually occur under the weather conditions with high temperature and low humidity. The value of 2-m relative humidity at NJ is relatively higher than those at SH and HZ and remains more stable. This extremely hot and

330   dry weather condition at SH, HZ, and NJ are successively relieved on August 12, 13 and 15, which

331   coincide well with the reduction of surface O_3 concentrations in Shanghai, Hangzhou, and Nanjing

332   (Fig. 2). With respect to the observed surface wind (Fig. 4b), the 10-m wind speed at SH and HZ is

333   comparatively lower during the period of the O_3 episode, while it is suddenly intensified after

334   August 12. Meanwhile, the wind direction is fluctuating from August 7 to 12, while it maintains

335   southeasterly wind after August 12 as well. The growth of wind speed is more distinct at SH, with

336   the maximum value of approximately 10 m/s. The wind speed at NJ has an obviously diurnal

337   variation from August 4 to 8, and the minimum value occurs on August 10.

338
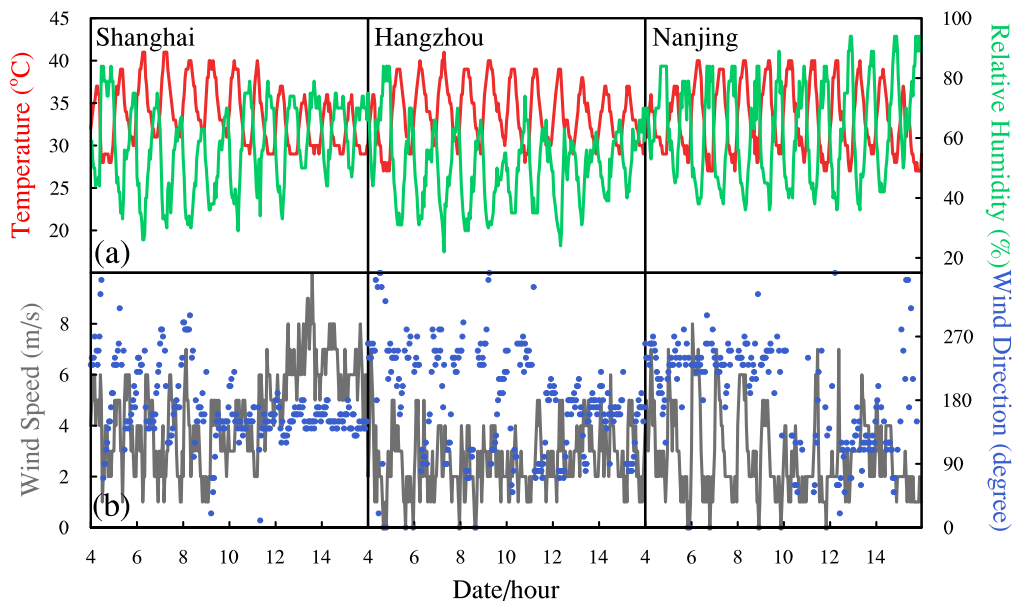
340 **Fig. 4. Temporal variations of the main meteorological parameters at Shanghai, Hangzhou and Nanjing**

341 **meteorological stations during August 4-15 2013, including (a) 2-m air temperature (the red solid line) and**

342 **2-m relative humidity (the green solid line); (b) 10-m wind speed (the gray solid line) and 10-m wind**

343 **direction (the blue scatter points).**

344

345   Fig. 5 displays the weather charts for the 500hPa layer over the East Asia at 00:00 (UTC) on

346   August 6, 8, 10, and 12 2013, which can illustrate the main synoptic patterns causing the O_3

347   pollution. Obviously, during the period of the selected O_3 episode, the whole YRD region is under

348   the control of the strong Western Pacific subtropical high, which is stronger and extends much

349   farther west than normal. The anomaly of the subtropical high might be the direct and leading

350   cause of the abnormally high temperature shown in Fig. 4a (Peng et al., 2014). The intensity of the

351 subtropical high is usually characterized by the area index, defined as the total number of grid

352 points that have geopotential heights of 588 decameters or greater in the region of 110-180°E and

353 northward of 10°N. As shown in Fig. 5, the 588-decameter area covers most of southeast China,

354 and the high pressure center (592-decameter area) is located in the southeastern coastal areas as

355 well as the surrounding sea areas, which means the subtropical high is very intensive. This high

356 pressure strengthens and remains over the YRD region for several days (from August 6 to 12),

357 implying that the air subsides to the ground. The downward air acts as a dome capping the

358 atmosphere, and helps to trap heat as well as air pollutants at the surface. Without the lift of air,

359 there is little convection and therefore little cumulus clouds or rains. The end result is a continual

360 accumulating of solar radiation and heat on the ground, which may greatly enhance the

361 photochemical reactions between the abundant build-up air pollutants.

362   The other weather system worthy of note is Typhoon Utor (shown in Fig. 5c and d). Typhoon

363 Utor is one of the strongest typhoons in the 2013 Pacific typhoon season. It is formed early on

364 August 8, develops into a tropical storm on August 9, undergoes an explosive

365 intensification within a half of day, and achieves typhoon status on early August 10. After landing

366 in Luzon of the Philippines on late August 11, it reemerges in the South China Sea on August 12.

367 Typhoon Utor hits the land of Guangdong Province in China on August 14, and thereby is finally

368 weakened into a tropical storm. In the end, it is ultimately dissipated on August 18. It was reported

369 that ozone episodes during the hot season are usually associated with the passage of tropical

370 cyclones close to the territory (Huang et al., 2005; Wang et al., 2006b; Jiang et al., 2008; Cheng et

371 al., 2014; Hung and Lo, 2015). When a site is at the front of moving typhoon system, it can be

372 controlled by the downward airflow induced by the typhoons' peripheral circulation. So, the

373 typhoon system can cause the local weather around the site with high temperature, low humidity,

374 strong solar radiation and small wind for a short time, before it is close enough to bring winds and

375 rains. All these changes of meteorological conditions can help to form the severe continuous O_3

376 pollution (Jiang et al., 2008). In this O_3 episode, the YRD region may be influenced by the

377 peripheral circulation of Typhoon Utor as well. Especially on August 10-11, the downward airflow

378 in the troposphere is significantly strengthened (shown in Fig. 7), which may enhance the build-up

379 of heat and air pollutants, and thereby result in worse air quality shown in Fig. 2.

380   Moreover, with the approaching of Typhoon Utor from August 12 to 14, the near-surface

381 breeze over the YRD region gradually turns to be the prevailing southeasterly or southerly wind

382 (Fig. 5d), with the highest wind speed up to 6-10 m/s in Shanghai (Fig. 4). The strengthened wind

383 can bring the clean marine air from ocean to inland, and thereby effectively mitigate the O_3

384 pollution. Meantime, Typhoon Utor also gradually affects the position and strength of the Western

385 Pacific subtropical high. As the typhoon continuously approaching and finally landing on

386 Guangdong, the high pressure system is forced to retreat easterly and move northwards. When the

387 high pressure center completely moves to the oceans, the YRD region is totally under the control

388 of the typhoon system. In the end, the hot weather is relieved and the O_3 pollution is mitigated.

389 The coastal cities in CSR are closer to the typhoon system, so they are firstly influenced during

390 this period. Thus, the wind at SH in CSR firstly changes, followed by HZ in CIR and NJ in NIR.

391 In the same way, 2-m air temperature and O_3 concentrations also successively decrease from

392 southeast (SH in CSR) to northwest (NJ in NIR) owing to the scavenging effect.

393
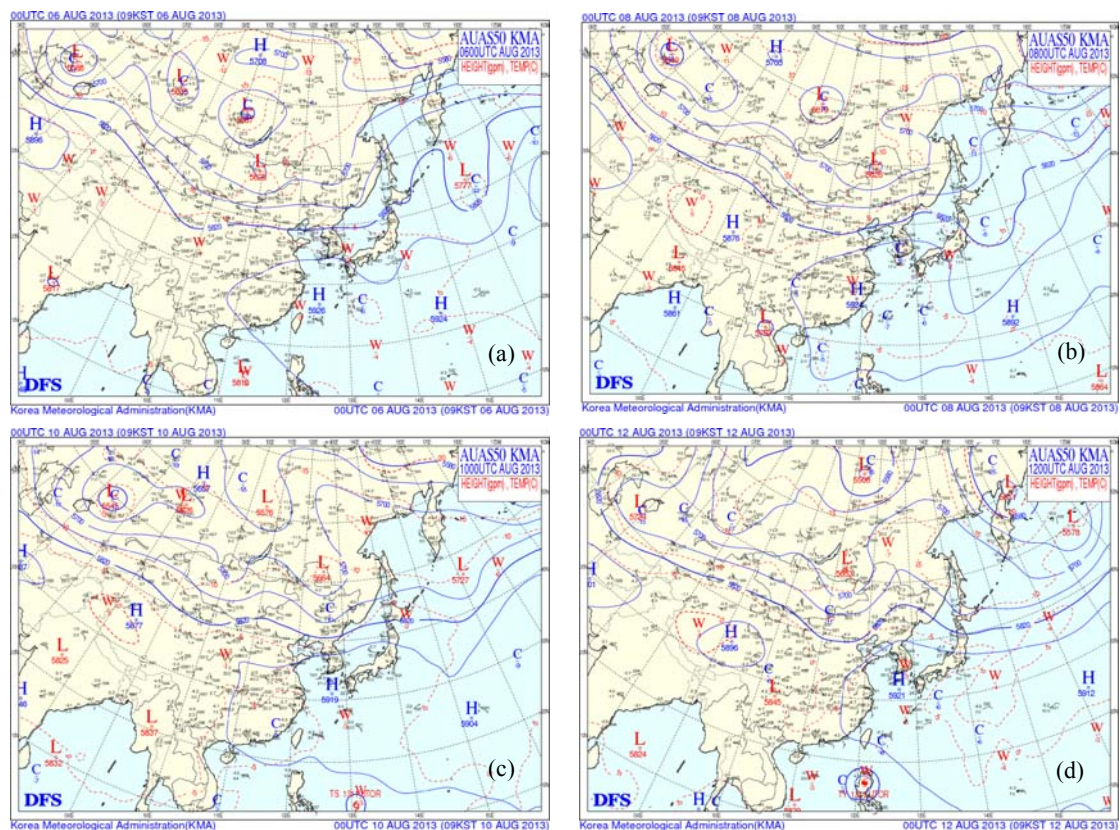
394 **Fig. 5. Weather charts at the 500hPa layer over the East Asia at 00:00 (UTC) on (a) August 6, (b) August 8,**

395 **(c) August 10, and (d) August 12 2013 (from Korea Meteorological Administration).**

396

397 **4 Modeling results and discussions**

4.1 Evaluation of model performance

To evaluate the simulation performance, the hourly modeling results during the period of August 4-15 2013 are compared with the observation records. Table 3 presents the performance statistics, including the values of the correlation coefficient (R), the normalized mean bias (NMB), and the root-mean-square error (RMSE), which are all calculated for 2-m air temperature (T_2), 2-m relative humidity (RH_2), 10-m wind speed ($Wspd_{10}$), 10-m wind direction ($Wdir_{10}$), surface ozone concentrations (O_3), and surface nitrogen dioxide concentrations (NO_2) in Shanghai (SH), Nanjing (NJ), and Hangzhou (HZ).

As indicated in Table 3, the simulated results of surface air temperature and relative humidity from WRF show good agreement with the observations. The highest correlation coefficient of 2-m air temperature (T_2) is found to be 0.91 at SH, followed by 0.84 at NJ and 0.80 at HZ (statistically significant at 95% confident level). The corresponding correlation coefficients for 2-m relative humidity (RH_2) are 0.85, 0.83 and 0.78, respectively. The values of RMSE for T_2 at SH, NJ and HZ are 4.15, 2.91and 3.09 ℃, and those for RH_2 are 19.3%, 9.41% and 13.96% respectively. Our simulation underestimates T_2 and overestimates RH_2 to some certain extent, with the values of NMB for T_2 at SH, NJ and HZ being -5.68%, -5.98% and -6.53%, and those for RH_2 being 12.64%, 4.52% and 16.36%. These biases might be attributed to the uncertainty caused by the SLAB scheme, which can underestimate temperature in summer (Liao et al., 2014). However, according to the relevant studies (Li et al., 2012; Liao et al., 2015; Xie et al., 2016a), this level of over- or under-estimation is still acceptable. The wind components are closely related to the transport processes. As shown in Table 3, our modeling results of wind speed and direction basically reflect the characteristics of wind fields. For 10-m wind speed (W_{spd10}), R is 077 at SH, 0.74 at NJ, and 0.75 at HZ, respectively. Though the values of NMB (1.53%, 5.92%, and 9.21%) and RMSE (2.18, 2.41 and 2.39) display that the simulated wind speeds are a little overestimated, the biases are still reasonable and acceptable. For 10-m wind direction (W_{dir10}), the simulated values also fit the observation records well, with the R values of 0.63 at SH, 0.57 at NJ and 0.58 at HZ. Comparing the mean values from SIM and OBS, we can find that WRF model generally simulates the prevailing wind direction during this period. In summary, the abovementioned performance statistics numbers illustrate that the WRF simulation can reflect the major characteristics of meteorological conditions of this O_3 episode, and the meteorological outputs can

428   be used in the pollutant concentration simulation.

429

430   **Table 3. Comparisons between the simulations and the observations at Shanghai, Nanjing and Hangzhou**
431   **stations during August 4-15 2013.**

Sites [a]	Vars [b]	Mean		R [e]	NMB [f]	RMSE [g]
		OBS [c]	SIM [d]			
SH	T_2 (°C)	33.27	31.38	0.91	-5.68%	4.15
	RH_2 (%)	57.91	65.23	0.85	12.64%	19.3
	$Wspd_{10}$ (m s⁻¹)	4.59	4.66	0.77	1.53%	2.18
	$Wdir_{10}$ (°)	176.34	182.57	0.63	3.53%	41.44
	O_3 (ppb)	87.77	82.5	0.81	-6.00%	38.79
	NO_2 (ppb)	29.01	38.25	0.54	31.85%	28.95
NJ	T_2 (°C)	32.95	30.98	0.84	-5.98%	2.91
	RH_2 (%)	63.28	66.14	0.83	4.52%	9.41
	$Wspd_{10}$ (m s⁻¹)	3.21	3.4	0.74	5.92%	2.41
	$Wdir_{10}$ (°)	197.68	194.58	0.57	-1.57%	71.19
	O_3 (ppb)	69.7	78.15	0.81	12.12%	36.8
	NO_2 (ppb)	41.44	40.09	0.61	-3.26%	22.4
HZ	T_2 (°C)	33.25	31.08	0.8	-6.53%	3.09
	RH_2 (%)	52.76	61.39	0.78	16.36%	13.96
	$Wspd_{10}$ (m s⁻¹)	3.04	3.32	0.75	9.21%	2.39
	$Wdir_{10}$ (°)	186.45	186.2	0.58	-0.13%	69.44
	O_3 (ppb)	76.57	84.51	0.83	10.37%	33.95
	NO_2 (ppb)	31.06	27.21	0.66	-12.40%	16.86

432   [a] Sites indicates the city where the observation sites locate, including Shanghai (SH), Nanjing (NJ), and Hangzhou
433   (HZ); [b] Vars indicates the variables under validation, including 2-m air temperature (T_2), 2-m relative humidity
434   (RH_2), 10-m wind speed ($Wspd_{10}$), 10-m wind direction ($Wdir_{10}$), ozone (O_3), and nitrogen dioxide (NO_2). The
435   words between the parentheses behind variables indicate the unit; [c] OBS indicates the observation data; [d] SIM
436   indicates the simulation results from WRF/CMAQ; [e] R indicates the correlation coefficients, with statistically
437   significant at 95% confident level; [f] NMB indicates the normalized mean bias; [g] RMSE indicates the
438   root-mean-square error.

439

440   Fig. 6 shows the comparisons between the modeling results from CMAQ and the observed

441   hourly concentrations of O_3 in Shanghai, Nanjing, and Hangzhou during August 4-15 2013.

442   Obviously, the observations and the simulated results present reasonable agreement at each site,

443   with the correlation coefficients of 0.81 to 0.83, NMB of -6% to 12.12%, RMSE of 33.95 to 38.79

444   ppb. Moreover, the simulation also reproduces the diurnal variation of O_3, which shows that the

445   concentration reaches its maximum at around noon time and gradually decreases to its minimum

after midnight. With respect to the O_3 precursor, comparisons of NO_2 concentrations between simulation results and observations show that the correlation coefficient at each city is about 0.6 (given in Table 3), which further prove that the process of O_3 formation is captured reasonable well over the YRD region and throughout the episode. However, CMAQ overestimates NO_2 and underestimates O_3 in Shanghai, while underestimates NO_2 and overestimates O_3 in Nanjing and Hangzhou. These biases of O_3 and NO_2 should mainly be attributed to the uncertainties in emissions of O_3 precursors (NO_x and VOC_s) (Li et al., 2012; Liao et al., 2015; Xie et al., 2016). Because of the VOC-sensitive O_3 chemistry in the daytime and NO_x titration at night in the YRD region (Xie et al., 2014), higher estimation of NO_x emission in Shanghai may lead to higher NO_2 and lower O_3 predictions, while lower NO_x estimations in Nanjing and Hangzhou may result in lower NO_2 and higher O_3 modeling results. The undervalued NO_2 and overvalued O_3 in Nanjing and Hangzhou can also be related with the overestimations in WS_{10} and the negative biases in T_2. Moreover, the uncertainties in nonlinear chemical reactions coupled in CMAQ may also have important effects on model predictions. For example, the modeling results cannot catch the low O_3 values observed at night in Nanjing and Hangzhou (Fig. 6), implying there may be some imperfections in the nocturnal chemistry of CMAQ. Nevertheless, the performance of CMAQ model is comparable to the other applications (Goncalves et al., 2009; Li et al., 2012; Zhu et al., 2016). Compared to these previous related studies, the simulation in this study attains an acceptable and satisfactory result. Thus, the consistency of simulation and observation demonstrates that the modeling results are capable of capturing and reproducing the characteristics and changes of photochemical pollutants, and can be used to provide valuable insights into the governing processes of this O_3 episode.
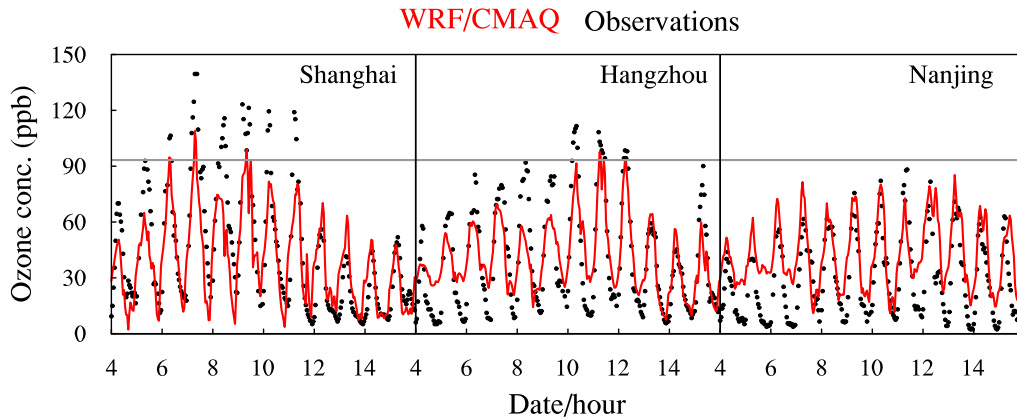
Fig. 6. Hourly variations of the observed and the simulated O$_3$ concentrations in Shanghai, Nanjing, and Hangzhou. The red solid lines show the modeling results, the black dot lines give the observations, and the solid gray lines represent the national standard for the hourly O$_3$ concentration, which is 200 μg/m^3.

4.2 Characteristics of the vertical airflows

Fig. 7 presents the daytime vertical wind velocity as well as the vertical distribution of O$_3$ concentrations from 116.5°E to 122.9°E along the latitude of 31.40°N (where Shanghai is located) during August 7-12 2013. The simulation results clearly illustrate that there are strong downward airflows over the YRD region during the period of the regional high-level O$_3$ pollution, which can be attributed to the fact that these areas are under the control of the subtropical high and the sinking airflow is predominant (as discussed in Sect. 3.2).

From August 7 to 9 2013, except for the mentioned regional sinking airflows, there are still some local thermal circulations continually occurring at the lower atmospheric layers (< 2 km) along the vertical cross-section of Hangzhou (HZ) - Nanjing (NJ). These circulations are related with urban heat islands. Usually high pressures are accompanied by more stagnant and fair dry weather, so the upward and the downward flows caused by urban-breeze circulations can easily appear in the urban areas. For the vertical distribution of O$_3$, its high concentrations (> 50 ppb) generally appear from the surface to 1.5km height above the cities. As discussed in Sect. 3.2, air pollutants tend to be trapped on the ground due to the regional sinking airflows. Moreover, the local circulations over the cities make the urban areas to be the convergence zones, and thereby more air pollutants can be accumulated in and around these cities. Under the weather conditions induced by the subtropical high, such as high air temperature, stronger solar radiation and less

water vapor, the chemical reactions between the build-up air pollutants can be enhanced to form the high-level O_3 pollution. Additionally, Fig. 7a-c also show that there are maximum O_3 concentrations (> 90 ppb) occurring near the surface in and around SH. This phenomenon should be explained by the fact that the coastal city (SH) is firstly affected by Typhoon Utor

From August 10 to 12, with the approaching of Typhoon Utor, the vertical air movements over the YRD region are not restricted at the lower atmosphere any more. As shown in Fig. 7d-f, there are stronger downward airflows from the surface to the top of troposphere. As discussed in Sect. 3.2, the YRD cities are at the front of the moving typhoon system, so the peripheral circulation of Typhoon Utor may enhance the sinking of atmosphere, which can lead to higher air temperature, lower humidity, and stronger solar radiation. Affected by the enhanced downward air movement as well as the relevant changes of meteorological conditions, O_3 concentrations over the YRD region maintain a high pollution level, with the O_3 concentrations over 60 ppb below the height of 1.5 km (Fig. 7d-f). Furthermore, the high value center of O_3 concentrations (>90 ppb) moves westwards during August 10-12, implying that the peripheral circulation of Typhoon Utor can drive the air from the coastal areas to the inland areas.
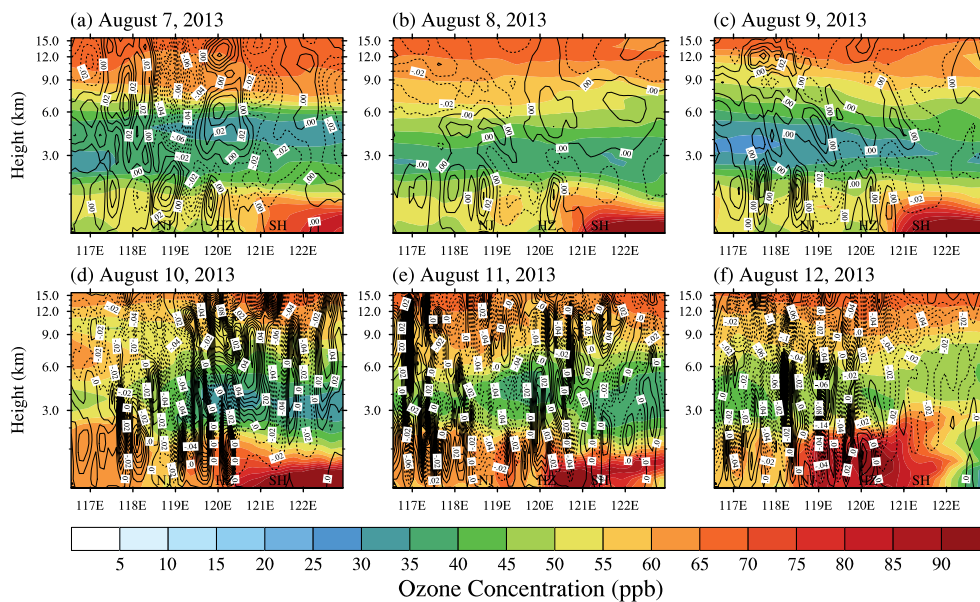
Fig. 7. Simulated daytime vertical wind velocity and vertical distribution of O_3 concentrations from 116.5°E to 122.9°E along the latitude of 31.40°N (where Shanghai is located) during August 7 to 12 2013. The marks of SH, HZ and NJ point out the longitudes of Shanghai, Hangzhou, and Nanjing, respectively. The dotted lines show the negative wind speeds and represent downward airflow, while the solid lines show the positive wind speeds and zero vertical velocity. The interval is 0.01 m/s.

515

The vertical changes of wind velocity and O_3 concentrations above Shanghai, Hangzhou and

Nanjing are further illustrated in Fig. 8. Similarly, the atmospheric subsidence can also be found in

the troposphere (usually occur at more than 1 km above the surface) during the period of the

high-level O_3 pollution. With respect to Shanghai, affected by the extremely high temperature,

more active photochemical reactions lead to higher O_3 concentrations in the whole atmospheric

boundary layer. The downward airflows induced by the subtropical high trap and enhance the

accumulation of surface O_3 as time passes. Thus, high O_3 concentrations are formed below 2 km

above the urban areas of Shanghai, and the high concentration centers occur near the surface

below 500 m. It is interesting that O_3 concentration on August 8 is comparatively lower, which can

be seen in Fig. 2 as well. This phenomenon can be explained by the fact that the transient upward

airflow occurs at above 300 m over Shanghai and inhibits the accumulation of the O_3 pollution at

the surface (shown in Fig. 8a). Additionally, Fig. 8a also presents the possible effects of Typhoon

Utor on the formation of O_3. On August 10, when the typhoon system approaches to the eastern

coastal areas of China, the sinking air above Shanghai is apparently strengthened, and thereby

enhances the intensity of O_3 pollution as well as the scope of the pollution. But after August 12,

when Typhoon Utor changes the wind and even impacts the subtropical high, high temperature is

alleviated and the build-up O_3 is transported to other places. Thus, the pollution is mitigated. As to

Hangzhou (Fig. 8b), from August 7 to 9, owing to weaker photochemical reactions, lower O_3

concentrations than that in Shanghai are found in the boundary layer. However, the O_3

concentration can exceed the national standard from August 10 to 12 (Fig. 2), which should be

influenced by the typhoon system. The influence process is similar to the above discussion for

Shanghai, that is, the upper downward airflows (over 1 km above the surface) are enhanced

significantly since August 10. But for Nanjing, the O_3 concentration does not exceed the national

O_3 standard during August 7-12 (Fig.2 and 8), which should be attributed to the fact that Nanjing

is far away from the coastal areas and thereby hardly affected by the downward flow in the

typhoon periphery. Though the O_3 concentration in Nanjing increases on August 12, it should

mainly be caused by the local photochemical reactions because the vertical movement below 2 km

above Nanjing is dominated by upward airflows.

544

545
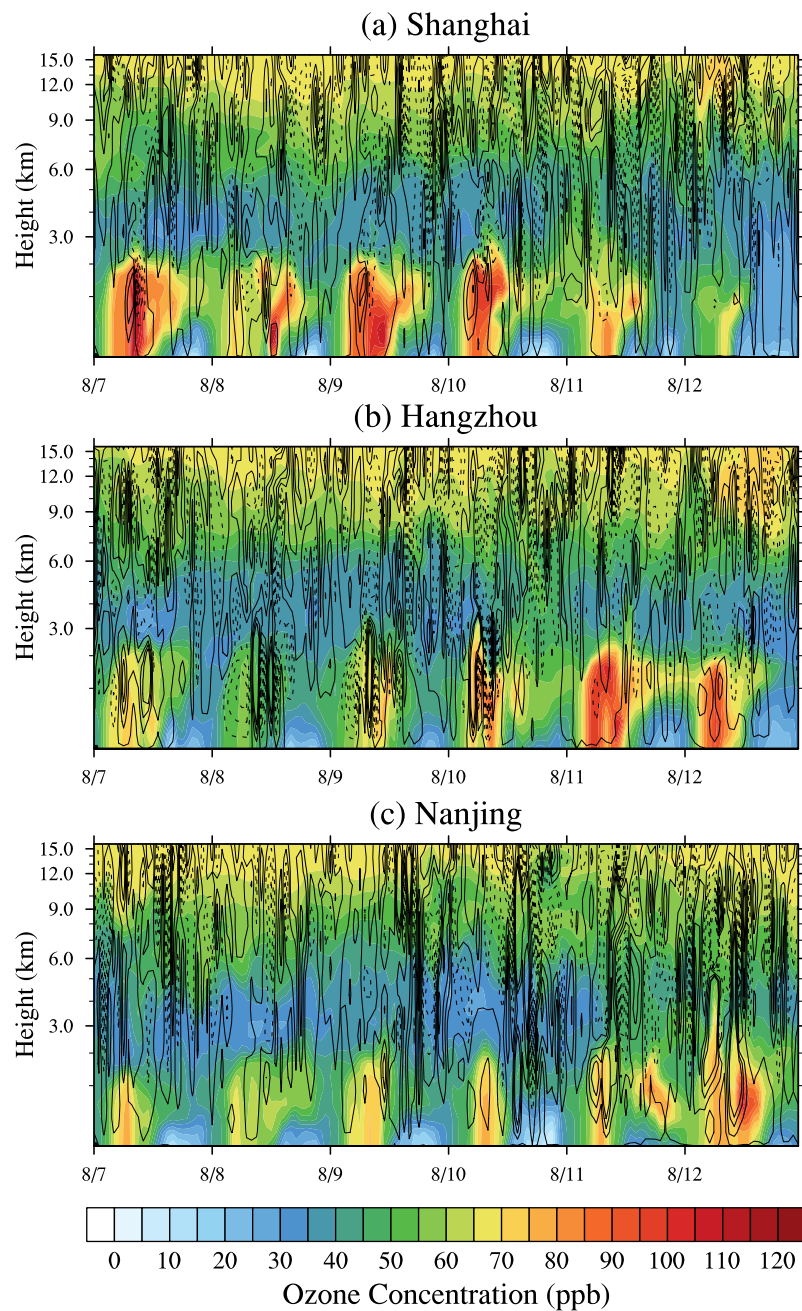
Fig. 8. Temporal variations of the vertical wind velocity and the vertical distribution of O_3 concentrations above (a) Shanghai, (b) Hangzhou and (c) Nanjing during August 7 to 12 2013. The dotted lines show the negative wind speeds and represent the downward airflows, while the solid lines show the positive wind speeds and zero vertical velocity. The interval is 0.005 m/s.

546
547
548
549
550
551

552 It is also should be mentioned that the near-surface vertical velocities around these cities are
553 much lower than those at higher altitudes (Fig.8). Especially in the planetary boundary layer (< 1
554 km), lots of zero-velocity lines appear near the ground. This phenomenon may be related with the
555 upward airflow caused by Urban Heat Islands. Thus, the maximum centers of O_3 occur near the
556 surface below 500 m, and the vertical diffusion process plays a more important role in the

557 accumulation of surface O_3. The essential role of the vertical diffusion process in the O_3 episode is
558 similar to that reported by Zhu et al. (2015).

559

560 **4.3 Process analysis for ozone formation**

561 **4.3.1 Typical cities in the YRD region**

562 Fig. 9 shows the daytime contributions of different atmospheric processes to the formation of

563 O_3 in Shanghai (SH), Nanjing (NJ), and Hangzhou (HZ) at the first modeling layer from August 4

564 to 15 2013. As shown in the figure, for all cities during this period, the major contributors to high

565 O_3 concentrations include the vertical diffusion (VDIF), the dry deposition (DDEP), the gas-phase

566 chemistry (CHEM), and the total advection (TADV). TADV is the sum of the horizontal advection

567 (HADV) and the vertical advection (ZADV). In this study, HADV and ZADV are considered

568 together as TADV because they are inevitably linked as the inseparable parts of air circulation. As

569 discussed in Sect. 3.2, the strong sinking air causes slow wind on the ground and little clouds in

570 the sky, so the contributions of horizontal diffusion (HDIF) and cloud processes (CLDS) are quite

571 small during this episode.

572 In the first layer of the urban areas of Shanghai (Fig. 9a), the averaged contributions from the

573 vertical diffusion (VDIF), the gas-phase chemistry (CHEM), the advection process (TADV), and

574 the dry deposition (DDEP) during the daytime of August 4-15 are 9.95, 10.10, -11.74 and -7.28

575 ppb/h, respectively. Obviously, VDIF and CHEM exhibit significant positive contributions to O_3

576 during most days, while TADV and DDEP mainly show the consumption contributions. The

577 sinking air caused by the weather system discussed in Sect. 3.2 can trap heat and air pollutants on

578 the ground, and make VDIF be the most import source of surface O_3. Meanwhile, the hotter and

579 dryer weather with more sunshine, above 40 $^{\circ}$C and comparatively low relative humidity (shown

580 in Fig. 4), which is related with the sinking air, can enhance the photochemical reactions. So,

581 CHEM can form more O_3 on the ground. Compared with the time series of CHEM and DDEP in

582 which there are no obvious fluctuations, the values of VDIF and TADV significantly change with

583 the time, with the daytime mean contributions varying from 3.99 to 28.45 ppb/h for VDIF and

584 from -2.56 to -28.13 ppb/h for TADV. These time variations should be related with the changes of

585 vertical air movement. For example, the value of VDIF on August 8 is only 3.99 ppb/h, which can

586 be attributed to the local transient upward airflow over Shanghai (shown in Fig. 8a). On August 10,

587 however, VDIF can contribute 28.45 ppb O_3 per hour, which may be related with the enhanced

588 downward air movement caused by the peripheral circulation of Typhoon Utor. Moreover, during

589 the high-level O_3 episode from August 7-12, the mean values for VDIF, CHEM, TADV and DDEP

590 are 13.41, 11.21, -8.37 and -14.74 ppb/h. But after August 12, the mean contributions of VDIF,

591 CHEM, TADV and DDEP decrease to 5.35, 9.53, -5.52 and -10.85 ppb/h. These reductions should

592 be related with the process that the subtropical high moves eastward and northward forced by

593 Typhoon Utor (Fig. 5d). By quantifying the relative importance of each process to O_3 formation,

594 the IPR analysis provides a fundamental explanation for the synthetical influence of the high

595 pressure and the typhoon system, which has been discussed in Sect. 3.2 and 4.1, and further

596 illustrates the exact mechanism.

597   Fig. 9b presents the result of IPR analysis for Hangzhou. During August 4-15, VDIF and

598 CHEM are the major source of surface O_3 with the average contribution of 5.36 ppb/h for VDIF

599 and 10.97 ppb/h for CHEM, while TADV and DDEP are two important sinks for O_3 with the

600 average contribution of -9.63 ppb/h for TADV and -5.14 ppb/h for DDEP. Synthetically impacted

601 by Western Pacific subtropical high and Typhoon Utor, the mean contributions during the O_3

602 episode (from August 7 to August 12) for VDIF, CHEM, TADV and DDEP increase to 7.21, 12.61,

603 -11.51 and -5.92 ppb/h, respectively. The highest VDIF contribution occurs on August 10-11, and

604 the over-standard of O_3 concentration appears on August 10-12 as well, which may be attributed to

605 the effect of typhoon's peripheral circulation, implying Typhoon Utor also plays an essential role

606 in the formation of O_3 pollution in Hangzhou. After Typhoon Utor approaches close enough to

607 Hangzhou, the wind direction is mainly dominated by the southeast wind (Fig. 4b), and the mean

608 values of VDIF, CHEM, TADV and DDEP finally decrease to 4.84, 10.08, -8.92 and -4.78 ppb/h,

609 respectively. In a word, Hangzhou is located close to Shanghai, so the temporal variations of VDIF,

610 CHEM, TADV and DDEP in Hangzhou are similar to those in Shanghai.

611   However, the similar variation pattern of VDIF, CHEM, TADV and DDEP occurring in

612 Shanghai and Hangzhou does not appear in Nanjing. As shown in Fig. 9c, the mean contributions

613 of VDIF, CHEM, TADV and DDEP to surface O_3 in Nanjing are 11.31, 9.55 -1.34 and -17.57

614 ppb/h during the whole period, while the values during 7-12 August are 10.32, 10.70, -0.99 and

615 -18.42 ppb/h. There are no apparent fluctuations or sudden increases of these contributors during

616 the period from August 4 to 15, so are the O_3 concentration (Fig. 2), temperature and relative

617   humidity (Fig. 4a), implying Nanjing is generally under the control of the Western Pacific

618   subtropical high and can hardly be affected by the typhoon system. As a typical city in the

619   northwest inland area of the YRD region (NIR), Nanjing is located far away from the sea, which

620   means it may not be easily affected by the peripheral circulation of the typhoon system.

621   Additionally, at the altitude of 500 m and 1500 m above Shanghai, Nanjing, and Hangzhou

622   (not shown), CHEM is also the major contributor to O_3 formation, with the values a litter lower

623   than those at the surface, suggesting that there are strong photochemical reactions in the whole

624   boundary layer of these YRD cities. In contrast, VDIF has an opposite effect in the middle of the

625   boundary layer, with the negative contributions for O_3 of -3.26 ppb/h in Shanghai, -2.37 ppb/h in

626   Hangzhou, and -3.21 ppb/h in Nanjing, respectively (not shown). The loss of O_3 at higher

627   atmospheric level caused by VDIF further proves the essential role of the downward vertical

628   movement in this O_3 episode.

629
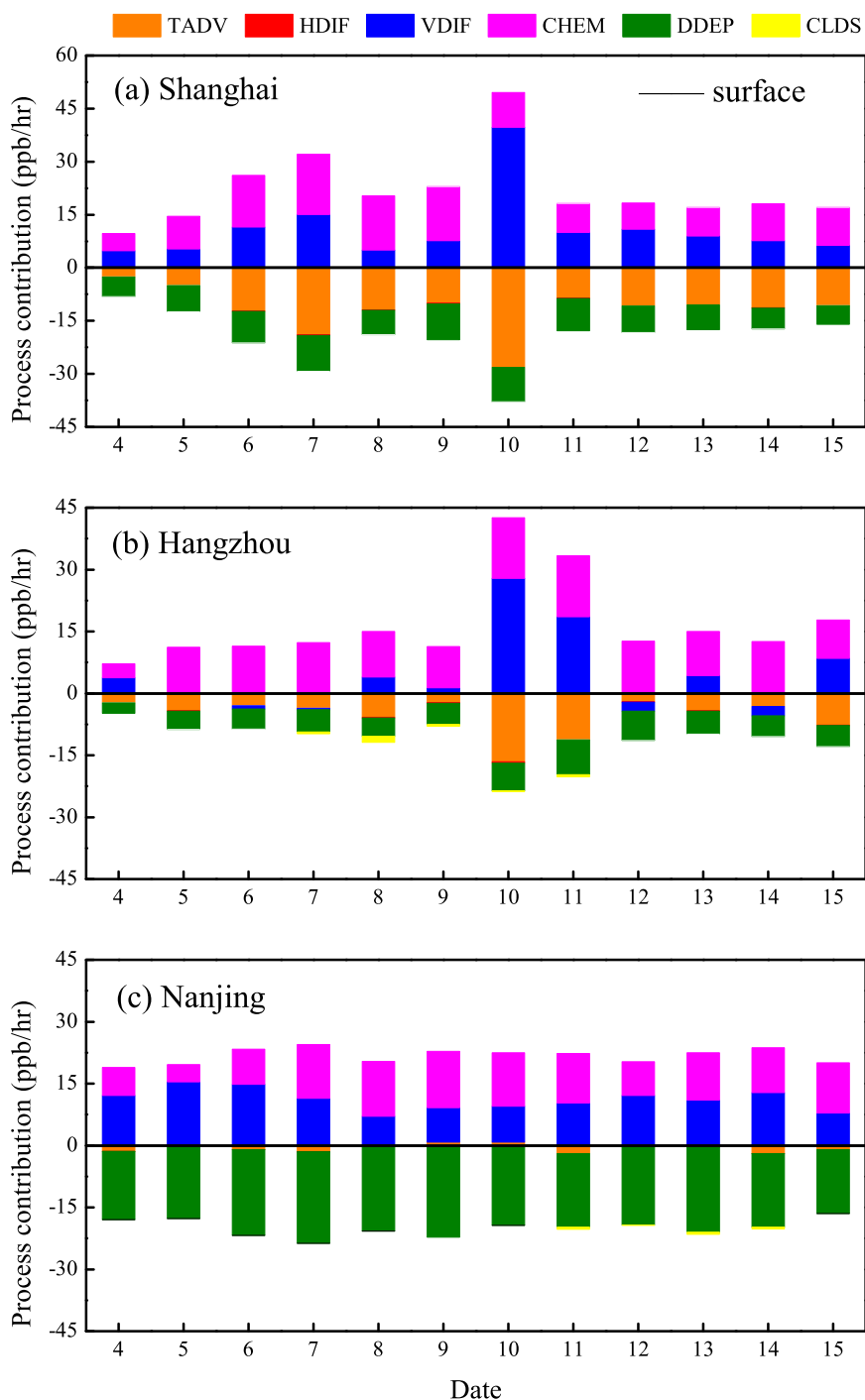
Fig. 9. Variations of the daytime mean values for the contributions of individual processes to O₃ formation in (a) Shanghai, (b) Hangzhou, and (c) Nanjing from August 4 to 15 2013 at the surface layer. The contributors include the total advection (TADV), the horizontal diffusion (HDIF), the vertical diffusion (VDIF), the gas-phase chemistry (CHEM), the dry deposition (DDEP), and the cloud processes with the aqueous chemistry (CLDS).

4.3.2 Spatial distribution of the contributors for the O₃ episode over the YRD region

Fig. 10 demonstrates the spatial distribution of the mean contributions of main processes

639 (VDIF, CHEM, DDEP and TADV) to the ozone formation at the lowest modeling layer in domain

640 3 during this high-level O_3 episode. The modeling results from 7 to 12 August are averaged to

641 provide the mean values.

642   Similar to the results shown in Fig. 9, Fig. 10 illustrates that the vertical diffusion (VDIF) and

643 the gas-phase chemistry (CHEM) exhibit significant positive contributions to O_3 over the YRD

644 region and the surrounding areas during the high-level O_3 episode. The contributions of VDIF in

645 domain 3 (Fig. 10a) range from 5 to 25 ppb/h, with the high values (> 20 ppb/h) occurring in the

646 southeast coastal areas. For CHEM (Fig. 10b), the contributions vary within the range of 0-15

647 ppb/h, with the high values over 10 ppb/h appearing in and around the big cities. As discussed

648 above, these regional positive contributions of VDIF and CHEM over domain 3 should be related

649 to the facts that the whole region is under the control of the Western Pacific subtropical high. With

650 respect to the higher contributions of CHEM in the urban areas, they should be attributed to the

651 spatial distribution of the emissions of O_3 precursors, which is also higher in the cities.

652 Furthermore, higher air temperature in the cities related with the urban heat island may enhance

653 the chemical reactions and form more O_3 in these areas as well.

654   For DDEP, it is the main critical factor of the consumption of O_3, with the negative

655 contributions varying from 0 to -25 ppb/h over the modeling domain 3 (Fig. 10c). Small values

656 usually occur on the water, which may be related with less air pollution over rivers, lakes and

657 oceans. High values can be found on land, especially in the southeast coastal areas. For the

658 contributions of TADV, the values in domain 3 range from -10 to 10 ppb/h, with the positive

659 contributions generally occurring on land while the negative ones appearing on the water (Fig.

660 10d). The maximum positive contributions of TADV are usually found along the boundary

661 between the land and the water, which should be explained by the facts that the land-sea breeze

662 circulations can play an important role in the redistribution of the formed O_3. On account of the

663 high-pressure system and so-caused sinking airflows in the YRD region, the background wind is

664 relatively weak in comparison to the local atmospheric circulation, thus the sea breeze can easily

665 bring more generated O_3 to the seashore.

666

667
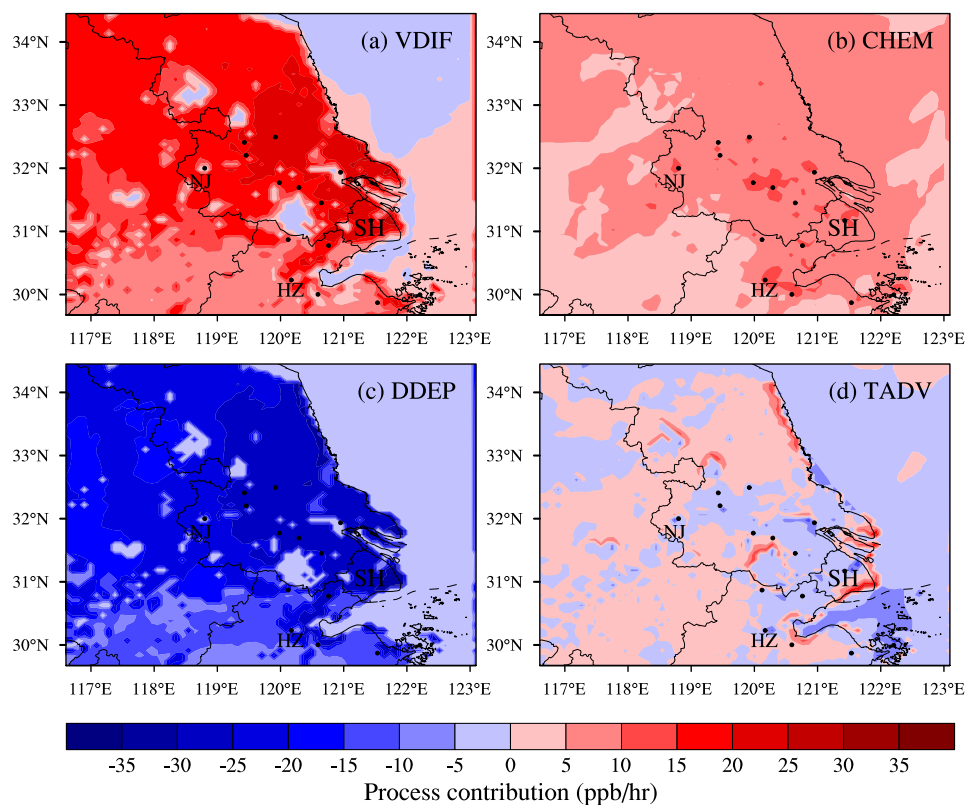
Fig. 9. The contributions of main processes to O$_3$ formation over the YRD region, including (a) vertical diffusion (VDIF), (b) gas chemistry (CHEM), (c) dry deposition (DDEP), and (d) total advection (TADV). The values are averaged from August 7 to 12 2013.

From the discussion in Section 3 and 4.2, it can be deduced that typhoon Utor plays an important role in the formation of ozone over the YRD region during August 10-12. To clearly clarify the effect of the typhoon system in this O$_3$ pollution episode, we firstly average the modeling results of VDIF, CHEM, DDEP and TADV during August 10-12 to show their contributions to O$_3$ formation when the typhoon system plays an important role. Secondly, the modeling results of these processes from August 7 to 9 are also averaged to provide their contributions when only the subtropical high dominates the episode. Finally, the differences of the contributions of VDIF, CHEM, DDEP and TADV between the period of August 7-9 and August 10-12 are calculated to reveal the role of the typhoon system in this severe high O$_3$ episode (Fig. 11). As shown in Fig. 11a, when YRD is affected by the peripheral circulation of Typhoon Utor, the contributions of VDIF over the YRD region increase by 0-15 ppb/h, with the higher increment values (> 30 ppb/h) occurring in the southeast coastal region (SCR) and center inland region (CIR),

685   implying that SCR and CIR can be largely affected by the peripheral subsidence airflows of the

686   typhoon system. As to the contributions of CHEM, the increases caused by the typhoon system are

687   0-5 ppb/h over the YRD region, and the higher increment also appears in the coastal areas (Fig.

688   11b). For DDEP, influenced by typhoon Utor, its negative contributions decrease up to -20 ppb/h,

689   with the largest reduction along the coastline (Fig. 11c). For TADV, with the approaching of

690   typhoon Utor, the contributions of TADV particularly decrease by 0-20 ppb/h, especially in the

691   southeast coastal region (Fig. 11d).

692   In all, during this high-level O$_3$ pollution episode, more active photochemical reactions and

693   the vertical diffusion play a significant role in the accumulation of surface O$_3$ over the YRD region.

694   The major driving factor should be the Western Pacific subtropical high. Moreover, the changes in

695   the contributions of VDIF, CHEM, DDEP, and TADV between August 7-9 and August 10-12

696   exhibit a similar spatial pattern with the high values mostly concentrating in the southeast coastal

697   areas (Fig. 12), implying the Typhoon Utor also plays a collaborative effect.

698
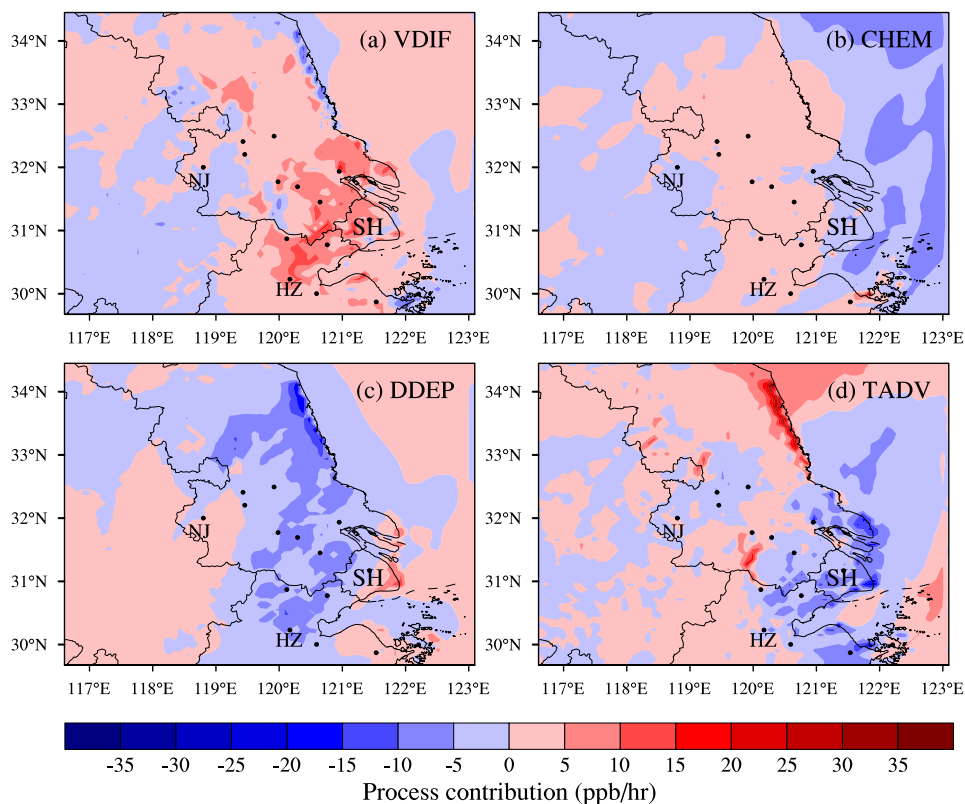
699

700   **Fig. 11. The difference of daytime mean contributions of main processes to O$_3$ formation over the YRD**

701   **region between the period of August 10-12 and August 7-9, including (a) vertical diffusion (VDIF), (b) gas**

702   **chemistry (CHEM), (c) dry deposition (DDEP), and (d) total advection (TADV) .**

5. Conclusions

In this study, the characteristics and the essential impact factors of a typical regional continuous O_3 pollution over the YRD region is investigated by means of observational analysis and numerical simulation. The episode lasted for nearly a week from August 7 to 12 2013, with the O_3 concentration exceeding the national air quality standard in more than half of the cities over the YRD region. The analysis of weather systems and the modeling results from WRF/CMAQ all illustrate that the continuous strong Western Pacific subtropical high is the leading factor of the abnormally high temperature weather and the heavy O_3 pollution, by inducing more sinking air to trap heat as well as air pollutants at the surface. Meanwhile, the development of this episode is closely related to the movement of Typhoon Utor as well. The temporal variations of the vertical wind velocity and O_3 concentrations show that when the YRD region is at the front of moving typhoon system, the downward airflow is enhanced in the boundary layer with fine weather, and thereby the air pollutants are trapped and accumulated near the surface. Moreover, in the last stage of the O_3 episode, the activity of Typhoon Utor weakens the strength of the subtropical high and forces it to retreat easterly and move northward, and the prevailing southeasterly surface wind related with the approaching of Typhoon Utor contributes to the mitigation of the O_3 pollution.

The Integrated Process Rate (IPR) analysis implemented in CMAQ is specially carried out to quantify the relative contributions of individual processes and give a fundamental explanation. During the high-level O_3 episode from August 7-12, the vertical diffusion (VDIF) and the gas-phase chemistry (CHEM) exhibit significant positive contributions to surface O_3 over the YRD region, with the high values over 20 ppb/h for VDIF and over 10 ppb/h for CHEM. The dry deposition (DDEP) is the major sink of surface O_3, while the total advection (TADV) can give the positive contribution on land and the negative contribution on the water. Moreover, on August 10-12, the YRD region is apparently affected by the periphery circulation of Typhoon Utor, with the contributions of VDIF over the YRD region increasing by 0-15 ppb/h, the contributions of CHEM increasing by 0-5 ppb/h, and the contributions of DDEP and TADV decreasing. Especially in the coastal cities, such as Shanghai and Hangzhou, the effects of the typhoon system are more obvious. In contrast, the cities in the northwest inland area of the YRD region, which are far away from the sea, can hardly be affected by the typhoon system. In the end, when the typhoon system

733 significantly weakens the high pressure system, the contributions of VDIF, CHEM, TADV, and

734 DDEP decrease to a low level in all cities.

735   WRF/CMAQ model system shows a relatively good performance in simulation of the O_3

736 episode, with the simulated meteorological conditions and air pollutant concentrations basically in

737 agreement with the observations in most YRD cities. Our results in this study can provide an

738 insight for the formation mechanism of regional O_3 pollution in East Asia, and help to forecast the

739 O_3 pollution synthetically impacted by the Western Pacific subtropical high and the tropical

740 cyclone system.

741

742 **Acknowledgments**

743 This study was supported by the National Natural Science Foundation of China (41475122,

744 91544230, 41575145), the National Special Fund for Environmental Protection Research in the

745 Public Interest (201409008), EU 7th Framework Marie Curie Actions IRSES project REQUA

746 (PIRSES-GA-2013-612671), and the National Science Foundation of Jiangsu Provence

747 (BE2015151). The authors would like to thank Hongli Wang from Shanghai Academy of

748 Environmental Sciences for providing VOCs observation data, Xiaoxun Xie for preliminary data

749 processing, and the anonymous reviewers for their constructive and precious comments on this

750 manuscript.

751

752 **References**

753 An, X., Zhu, T., Wang, Z., Li, C., and Wang, Y.: A modeling analysis of a heavy air pollution episode occurred in
754   Beijing, Atmos Chem Phys, 7, 3103-3114, 2007.

755 Byun, D., and Schere, K. L.: Review of the governing equations, computational algorithms, and other components
756   of the models-3 Community Multiscale Air Quality (CMAQ) modeling system, Appl Mech Rev, 59, 51-77,
757   10.1115/1.2128636, 2006.

758 Chan, C. K., and Yao, X.: Air pollution in mega cities in China, Atmos Environ, 42, 1-42,
759   10.1016/j.atmosenv.2007.09.003, 2008.

760 Chen, F., and Dudhia, J.: Coupling an advanced land surface-hydrology model with the Penn State-NCAR MM5
761   modeling system. Part I: Model implementation and sensitivity, Mon Weather Rev, 129, 569-585, Doi
762   10.1175/1520-0493(2001)129<0569:Caalsh>2.0.Co;2, 2001.

763 Chen, D., Zhou, B., Beirle, S., Chen, L. M., and Wagner, T.: Tropospheric NO2 column densities deduced from
764   zenith-sky DOAS measurements in Shanghai, China, and their application to satellite validation, Atmos Chem
765   Phys, 9, 3641-3662, 2009.

766 Cheng, W. L., Lai, L. W., Den, W., Wu, M. T., Hsueh, C. A., Lin, P. L., Pai, C. L., and Yan, Y. L.: The

767   relationship between typhoons' peripheral circulation and ground-level ozone concentrations in central Taiwan,

768   Environ Monit Assess, 186, 791-804, 10.1007/s10661-013-3417-7, 2014.

769 Chiqueto, J., Silva, M. E. S.: São Paulo "Surface Ozone Layer" and the atmosphere: characteristics of tropospheric

770   ozone concentrations in the city and how the atmosphere influences them, VDM Verlag Dr. Muller,

771   Saarbrücken, 2010.

772 Ding, A. J., Fu, C. B., Yang, X. Q., Sun, J. N., Zheng, L. F., Xie, Y. N., Herrmann, E., Nie, W., Petaja, T.,

773   Kerminen, V. M., and Kulmala, M.: Ozone and fine particle in the western Yangtze River Delta: an overview

774   of 1 yr data at the SORPES station, Atmos Chem Phys, 13, 5813-5830, 10.5194/acp-13-5813-2013, 2013.

775 Duan, J. C., Tan, J. H., Yang, L., Wu, S., and Hao, J. M.: Concentration, sources and ozone formation potential of

776   volatile organic compounds (VOCs) during ozone episode in Beijing, Atmos Res, 88, 25-35,

777   10.1016/j.atmosres.2007.09.004, 2008.

778 Emmons, L. K., Walters, S., Hess, P. G., Lamarque, J. F., Pfister, G. G., Fillmore, D., Granier, C., Guenther, A.,

779   Kinnison, D., Laepple, T., Orlando, J., Tie, X., Tyndall, G., Wiedinmyer, C., Baughcum, S. L., and Kloster, S.:

780   Description and evaluation of the Model for Ozone and Related chemical Tracers, version 4 (MOZART-4),

781   Geosci Model Dev, 3, 43-67, 2010.

782 Fann, N., and Risley, D.: The public health context for PM2.5 and ozone air quality trends, Air Qual Atmos Hlth, 6,

783   1-11, 10.1007/s11869-010-0125-0, 2013.

784 Feng, Z. W., Jin, M. H., Zhang, F. Z., and Huang, Y. Z.: Effects of ground-level ozone (O-3) pollution on the

785   yields of rice and winter wheat in the Yangtze River Delta, J Environ Sci-China, 15, 360-362, 2003.

786 Foley, K. M., Roselle, S. J., Appel, K. W., Bhave, P. V., Pleim, J. E., Otte, T. L., Mathur, R., Sarwar, G., Young, J.

787   O., Gilliam, R. C., Nolte, C. G., Kelly, J. T., Gilliland, A. B., and Bash, J. O.: Incremental testing of the

788   Community Multiscale Air Quality (CMAQ) modeling system version 4.7, Geosci Model Dev, 3, 205-226,

789   2010.

790 Gao, J. H., Bin, Z., Xiao, H., Kang, H. Q., Hou, X. W., and Shao, P.: A case study of surface ozone source

791   apportionment during a high concentration episode, under frequent shifting wind conditions over the Yangtze

792   River Delta, China, Sci Total Environ, 544, 853-863, 10.1016/j.scitotenv.2015.12.039, 2016.

793 Geng, F. H., Tie, X. X., Xu, J. M., Zhou, G. Q., Peng, L., Gao, W., Tang, X., and Zhao, C. S.: Characterizations of

794   ozone, NOx, and VOCs measured in Shanghai, China, Atmos Environ, 42, 6873-6883,

795   10.1016/j.atmosenv.2008.05.045, 2008.

796 Goncalves, M., Jimenez-Guerrero, P., and Baldasano, J. M.: Contribution of atmospheric processes affecting the

797   dynamics of air pollution in South-Western Europe during a typical summertime photochemical episode,

798   Atmos Chem Phys, 9, 849-864, 2009.

799 Grell, G. A., and Devenyi, D.: A generalized approach to parameterizing convection combining ensemble and data

800   assimilation techniques, Geophys Res Lett, 29, Artn 169310.1029/2002gl015311, 2002.

801 Guo, H., Jiang, F., Cheng, H. R., Simpson, I. J., Wang, X. M., Ding, A. J., Wang, T. J., Saunders, S. M., Wang, T.,

802   Lam, S. H. M., Blake, D. R., Zhang, Y. L., and Xie, M.: Concurrent observations of air pollutants at two sites

803   in the Pearl River Delta and the implication of regional transport, Atmos Chem Phys, 9, 7343-7360, 2009.

804 Han, S. Q., Bian, H., Feng, Y. C., Liu, A. X., Li, X. J., Zeng, F., and Zhang, X. L.: Analysis of the Relationship

805   between O-3, NO and NO2 in Tianjin, China, Aerosol Air Qual Res, 11, 128-139, 10.4209/aaqr.2010.07.0055,

806   2011.

807 Hong, S. Y., Dudhia, J., and Chen, S. H.: A revised approach to ice microphysical processes for the bulk

808   parameterization of clouds and precipitation, Mon Weather Rev, 132, 103-120, Doi

809   10.1175/1520-0493(2004)132<0103:Aratim>2.0.Co;2, 2004.

810 Hong, S. Y., Noh, Y., and Dudhia, J.: A new vertical diffusion package with an explicit treatment of entrainment

811   processes, Mon Weather Rev, 134, 2318-2341, Doi 10.1175/Mwr3199.1, 2006.

812   Huang, J. P., Fung, J. C. H., Lau, A. K. H., and Qin, Y.: Numerical simulation and process analysis of
813   typhoon-related ozone episodes in Hong Kong, J Geophys Res-Atmos, 110, Artn
814   D0530110.1029/2004jd004914, 2005.

815   Huang, J. P., Fung, J. C. H., and Lau, A. K. H.: Integrated processes analysis and systematic meteorological
816   classification of ozone episodes in Hong Kong, J Geophys Res-Atmos, 111, Artn
817   D2030910.1029/2005jd007012, 2006.

818   Hung, C. H., and Lo, K. C.: Relationships between Ambient Ozone Concentration Changes in Southwestern
819   Taiwan and Invasion Tracks of Tropical Typhoons, Adv Meteorol, Artn 40297610.1155/2015/402976, 2015.

820   Jenkin, M. E., and Clemitshaw, K. C.: Ozone and other secondary photochemical pollutants: chemical processes
821   governing their formation in the planetary boundary layer, Atmos Environ, 34, 2499-2527, Doi
822   10.1016/S1352-2310(99)00478-1, 2000.

823   Jiang, F., Wang, T. J., Wang, T. T., Xie, M., and Zhao, H.: Numerical modeling of a continuous photochemical
824   pollution episode in Hong Kong using WRF-chem, Atmos Environ, 42, 8717-8727,
825   10.1016/j.atmosenv.2008.08.034, 2008.

826   Jiang, F., Zhou, P., Liu, Q., Wang, T. J., Zhuang, B. L., and Wang, X. Y.: Modeling tropospheric ozone formation
827   over East China in springtime, J Atmos Chem, 69, 303-319, 10.1007/s10874-012-9244-3, 2012.

828   Kim, H. J., and Wang, B.: Sensitivity of the WRF Model Simulation of the East Asian Summer Monsoon in 1993
829   to Shortwave Radiation Schemes and Ozone Absorption, Asia-Pac J Atmos Sci, 47, 167-180,
830   10.1007/s13143-011-0006-y, 2011.

831   Lam, K. S., Wang, T. J., Wu, C. L., and Li, Y. S.: Study on an ozone episode in hot season in Hong Kong and
832   transboundary air pollution over Pearl River Delta region of China, Atmos Environ, 39, 1967-1977,
833   10.1016/j.atmosenv.2004.11.023, 2005.

834   Landry, J. S., Neilson, E. T., Kurz, W. A., and Percy, K. E.: The impact of tropospheric ozone on landscape-level
835   merchantable biomass and ecosystem carbon in Canadian forests, Eur J Forest Res, 132, 71-81,
836   10.1007/s10342-012-0656-z, 2013.

837   Li, L., Chen, C. H., Huang, C., Huang, H. Y., Zhang, G. F., Wang, Y. J., Chen, M. H., Wang, H. L., Chen, Y. R.,
838   Streets, D. G., and Fu, J. M.: Ozone sensitivity analysis with the MM5-CMAQ modeling system for Shanghai,
839   J Environ Sci-China, 23, 1150-1157, 10.1016/S1001-0742(10)60527-X, 2011.

840   Li, L., Chen, C. H., Huang, C., Huang, H. Y., Zhang, G. F., Wang, Y. J., Wang, H. L., Lou, S. R., Qiao, L. P.,
841   Zhou, M., Chen, M. H., Chen, Y. R., Streets, D. G., Fu, J. S., and Jang, C. J.: Process analysis of regional
842   ozone formation over the Yangtze River Delta, China using the Community Multi-scale Air Quality modeling
843   system, Atmos Chem Phys, 12, 10971-10987, 10.5194/acp-12-10971-2012, 2012.

844   Li, M. M., Song, Y., Huang, X., Li, J. F., Mao, Y., Zhu, T., Cai, X. H., and Liu, B.: Improving mesoscale modeling
845   using satellite-derived land surface parameters in the Pearl River Delta region, China, J Geophys Res-Atmos,
846   119, 6325-6346, 10.1002/2014JD021871, 2014.

847   Li, M. M., Song, Y., Mao, Z. C., Liu, M. X., and Huang, X.: Impacts of thermal circulations induced by
848   urbanization on ozone formation in the Pearl River Delta region, China, Atmos Environ, 127, 382-392,
849   10.1016/j.atmosenv.2015.10.075, 2016.

850   Liao, J. B., Wang, T. J., Wang, X. M., Xie, M., Jiang, Z. Q., Huang, X. X., and Zhu, J. L.: Impacts of different
851   urban canopy schemes in WRF/Chem on regional climate and air quality in Yangtze River Delta, China,
852   Atmos Res, 145, 226-243, 10.1016/j.atmosres.2014.04.005, 2014.

853   Liao, J. B., Wang, T. J., Jiang, Z. Q., Zhuang, B. L., Xie, M., Yin, C. Q., Wang, X. M., Zhu, J. L., Fu, Y., and
854   Zhang, Y.: WRF/Chem modeling of the impacts of urban expansion on regional climate and air pollutants in

855   Yangtze River Delta, China, Atmos Environ, 106, 204-214, 10.1016/j.atmosenv.2015.01.059, 2015.

856   Liu, X. H., Zhang, Y., Xing, J., Zhang, Q. A., Wang, K., Streets, D. G., Jang, C., Wang, W. X., and Hao, J. M.:
857   Understanding of regional air pollution over China using CMAQ, part II. Process analysis and sensitivity of
858   ozone and particulate matter to precursor emissions, Atmos Environ, 44, 3719-3727,
859   10.1016/j.atmosenv.2010.03.036, 2010.

860   Liu, Q., Lam, K. S., Jiang, F., Wang, T. J., Xie, M., Zhuang, B. L., and Jiang, X. Y.: A numerical study of the
861   impact of climate and emission changes on surface ozone over South China in autumn time in 2000-2050,
862   Atmos Environ, 76, 227-237, 10.1016/j.atmosenv.2013.01.030, 2013.

863   Lou, S. J., Liao, H., and Zhu, B.: Impacts of aerosols on surface-layer ozone concentrations in China through
864   heterogeneous reactions and changes in photolysis rates, Atmos Environ, 85, 123-138,
865   10.1016/j.atmosenv.2013.12.004, 2014.

866   Lu, W. Z., and Wang, X. K.: Evolving trend and self-similarity of ozone pollution in central Hong Kong ambient
867   during 1984-2002, Sci Total Environ, 357, 160-168, 10.1016/j.scitotenv.2005.03.015, 2006.

868   Ma, J. Z., Xu, X. B., Zhao, C. S., and Yan, P.: A review of atmospheric chemistry research in China:
869   Photochemical smog, haze pollution, and gas-aerosol interactions, Adv Atmos Sci, 29, 1006-1026,
870   10.1007/s00376-012-1188-7, 2012.

871   Mlawer, E. J., Taubman, S. J., Brown, P. D., Iacono, M. J., and Clough, S. A.: Radiative transfer for
872   inhomogeneous atmospheres: RRTM, a validated correlated-k model for the longwave, J Geophys Res-Atmos,
873   102, 16663-16682, Doi 10.1029/97jd00237, 1997.

874   Monin, A. S., Obukhov, A.M.: Basic laws of turbulent mixing in the surface layer of the atmosphere,
875   Contributions of the Geophysical Institute of the Slovak Academy of Sciences 151, 163-187, 1954.

876   Peng, J. B.: An Investigation of the Formation of the Heat Wave in Southern China in Summer 2013 and the
877   Relevant Abnormal Subtropical High Activities, Atmospheric & Oceanic Science Letters, 7, 286-290, 2014.

878   Ran, L., Zhao, C. S., Geng, F. H., Tie, X. X., Tang, X., Peng, L., Zhou, G. Q., Yu, Q., Xu, J. M., and Guenther, A.:
879   Ozone photochemical production in urban Shanghai, China: Analysis based on ground level observations, J
880   Geophys Res-Atmos, 114, Artn D1530110.1029/2008jd010752, 2009.

881   Shao, M., Zhang, Y. H., Zeng, L. M., Tang, X. Y., Zhang, J., Zhong, L. J., and Wang, B. G.: Ground-level ozone
882   in the Pearl River Delta and the roles of VOC and NOx in its production, J Environ Manage, 90, 512-518,
883   10.1016/j.jenvman.2007.12.008, 2009.

884   Shi, C. Z., Wang, S. S., Liu, R., Zhou, R., Li, D. H., Wang, W. X., Li, Z. Q., Cheng, T. T., and Zhou, B.: A study
885   of aerosol optical properties during ozone pollution episodes in 2013 over Shanghai, China, Atmos Res, 153,
886   235-249, 10.1016/j.atmosres.2014.09.002, 2015.

887   Sillman, S.: The relation between ozone, NOx and hydrocarbons in urban and polluted rural environments, Atmos
888   Environ, 33, 1821-1845, Doi 10.1016/S1352-2310(98)00345-8, 1999.

889   State Environmental Protection Administration of China: China National Environmental Protection Standard:
890   Automated Methods for Ambient Air Quality Monitoring, China Environmental Science Press, Beijing, 2006.

891   Tang, W. Y., Zhao, C. S., Geng, F. H., Peng, L., Zhou, G. Q., Gao, W., Xu, J. M., and Tie, X. X.: Study of ozone
892   "weekend effect" in Shanghai, Sci China Ser D, 51, 1354-1360, 10.1007/s11430-008-0088-2, 2008.

893   Tang, G., Li, X., Wang, Y., Xin, J., and Ren, X.: Surface ozone trend details and interpretations in Beijing,
894   2001-2006, Atmos Chem Phys, 9, 8813-8823, 2009.

895   Tu, J., Xia, Z. G., Wang, H. S., and Li, W. Q.: Temporal variations in surface ozone and its precursors and
896   meteorological effects at an urban site in China, Atmos Res, 85, 310-337, 10.1016/j.atmosres.2007.02.003,
897   2007.

898   Wang, H. L., Chen, C. H., Wang, Q., Huang, C., Su, L. Y., Huang, H. Y., Lou, S. R., Zhou, M., Li, L., and Qiao, L.

P.: Chemical loss of volatile organic compounds and its impact on the source analysis through a two-year continuous measurement, Atmospheric Environment, 80, 488-498, 2013.

Wang, H. X., Zhou, L. J., and Tang, X. Y.: Ozone concentrations in rural regions of the Yangtze Delta in China, J Atmos Chem, 54, 255-265, 10.1007/s10874-006-9024-z, 2006a.

Wang, T. J., Lam, K. S., Xie, M., Wang, X. M., Carmichael, G., and Li, Y. S.: Integrated studies of a photochemical smog episode in Hong Kong and regional transport in the Pearl River Delta of China, Tellus B, 58, 31-40, 10.1111/j.1600-0889.2005.00172.x, 2006b.

Wang, X. M., Lin, W. S., Yang, L. M., Deng, R. R., and Lin, H.: A numerical study of influences of urban land-use change on ozone distribution over the Pearl River Delta region, China, Tellus B, 59, 633-641, 10.1111/j.1600-0889.2007.00271.x, 2007.

Wang, T., Wei, X. L., Ding, A. J., Poon, C. N., Lam, K. S., Li, Y. S., Chan, L. Y., and Anson, M.: Increasing surface ozone concentrations in the background atmosphere of Southern China, 1994-2007, Atmos Chem Phys, 9, 6217-6227, 2009a.

Wang, X. M., Chen, F., Wu, Z. Y., Zhang, M. G., Tewari, M., Guenther, A., and Wiedinmyer, C.: Impacts of Weather Conditions Modified by Urban Expansion on Surface Ozone: Comparison between the Pearl River Delta and Yangtze River Delta Regions, Adv Atmos Sci, 26, 962-972, 10.1007/s00376-009-8001-2, 2009b.

Wei, X. L., Liu, Q., Lam, K. S., and Wang, T. J.: Impact of precursor levels and global warming on peak ozone concentration in the Pearl River Delta Region of China, Adv Atmos Sci, 29, 635-645, 10.1007/s00376-011-1167-4, 2012.

Xie, M., Wang, T.J., Jiang, F., Yang, X.Q.: Modeling of natural NOx and VOC emissions and their effects on tropospheric photochemistry in China, Environ. Sci. China, 28, 31-40, 2007.

Xie, M., Li, S., Jiang, F., and Wang, T. J.: Methane emissions from terrestrial plants over China and their effects on methane concentrations in lower troposphere, Chinese Sci Bull, 54, 304-310, 10.1007/s11434-008-0402-6, 2009.

Xie, M., Zhu, K. G., Wang, T. J., Yang, H. M., Zhuang, B. L., Li, S., Li, M. G., Zhu, X. S., and Ouyang, Y.: Application of photochemical indicators to evaluate ozone nonlinear chemistry and pollution control countermeasure in China, Atmos Environ, 99, 466-473, 10.1016/j.atmosenv.2014.10.013, 2014.

Xie, M., Liao, J., Wang, T., Zhu, K., Zhuang, B., Han, Y., Li, M., Li, S.: Modeling of the anthropogenic heat flux and its effect on regional meteorology and air quality over theYangtze River Delta region, China, Atmos. Chem. Phys., 16, 6071-6089, 10.5194/acp-16-6071-2016, 2016a.

Xie, M., Zhu, K. G., Wang, T. J., Chen, P. L., Han, Y., Li, S., Zhuang, B. L., and Shu, L.: Temporal characterization and regional contribution to O-3 and NOx at an urban and a suburban site in Nanjing, China, Sci Total Environ, 551, 533-545, 10.1016/j.scitotenv.2016.02.047, 2016b.

Yarwood, G., Rao, S., Yocke, M., Whitten G.: Updates to the Carbon Bond chemical mechanism: CB05., Final Report to the U.S. EPA, RT-0400675, 2005.

Zhang, X. Y., Zhang, P., Zhang, Y., Li, X. J., and Qiu, H.: The trend, seasonal cycle, and sources of tropospheric NO2 over China during 1997-2006 based on satellite measurement, Sci China Ser D, 50, 1877-1884, 10.1007/s11430-007-0141-6, 2007.

Zhang, Y. H., Su, H., Zhong, L. J., Cheng, Y. F., Zeng, L. M., Wang, X. S., Xiang, Y. R., Wang, J. L., Gao, D. F., Shao, M., Fan, S. J., and Liu, S. C.: Regional ozone pollution and observation-based approach for analyzing ozone-precursor relationship during the PRIDE-PRD2004 campaign, Atmos Environ, 42, 6203-6218, 10.1016/j.atmosenv.2008.05.002, 2008.

Zhang, Q., Streets, D. G., Carmichael, G. R., He, K. B., Huo, H., Kannari, A., Klimont, Z., Park, I. S., Reddy, S., Fu, J. S., Chen, D., Duan, L., Lei, Y., Wang, L. T., and Yao, Z. L.: Asian emissions in 2006 for the NASA

943   INTEX-B mission, Atmos Chem Phys, 9, 5131-5153, 2009.

944   Zhu, B., Kang, H. Q., Zhu, T., Su, J. F., Hou, X. W., and Gao, J. H.: Impact of Shanghai urban land surface forcing

945   on downstream city ozone chemistry, J Geophys Res-Atmos, 120, 4340-4351, 10.1002/2014JD022859, 2015.

946